The transcription factor Pdr802 regulates Titan cell formation, quorum sensing, and pathogenicity of *Cryptococcus neoformans*

Julia C. V. Reuwsaat[1,2], Daniel P. Agustinho[2], Heryk Motta[1], Holly Brown[2], Andrew L. Chang[2], Michael R. Brent[3], Livia Kmetzsch[1,4,5], and Tamara L. Doering[2,5].

[1]Molecular Biology of Pathogens Laboratory, Biotechnology Center, Universidade Federal do Rio Grande do Sul, Porto Alegre, Brazil.

[2]Department of Molecular Microbiology, Washington University School of Medicine, St. Louis, Missouri, USA.

[3]Center for Genome Sciences and Systems Biology, Washington University School of Medicine, and Departments of Computer Science and Genetics, Washington University, St. Louis, Missouri, USA.

[4]Department of Molecular Biology and Biotechnology, Universidade Federal do Rio Grande do Sul, Porto Alegre, Brazil.

[5]Corresponding authors: livia.kmetzsch@ufrgs.br, doering@wustl.edu

Running head: The role of Pdr802 in *Cryptococcus neoformans* virulence.

ABSTRACT

Cryptococcus neoformans is a ubiquitous, opportunistic fungal pathogen that kills almost 200,000 people worldwide each year. It is acquired when mammalian hosts inhale the infectious propagules; these are deposited in the lung and, in the context of immunocompromise, may disseminate to the brain and cause lethal meningoencephalitis. Once inside the host, *C. neoformans* undergoes a variety of adaptive processes, including secretion of virulence factors, expansion of a polysaccharide capsule that impedes phagocytosis, and the production of giant (Titan) cells. The transcription factor Pdr802 is one regulator of these responses to the host environment. Expression of the corresponding gene is highly induced under host-like conditions *in vitro* and is critical for *C. neoformans* dissemination and virulence in a mouse model of infection. Direct targets of Pdr802 include the quorum sensing proteins Pqp1, Opt1 and Liv3; the transcription factors Stb4, Zfc3 and Bzp4, which regulate cryptococcal brain infectivity and capsule thickness; the calcineurin targets Had1 and Crz1, important for cell wall remodeling and *C. neoformans* virulence; and additional genes related to resistance to host temperature and oxidative stress, and to urease activity. Notably, cryptococci engineered to lack Pdr802 showed a dramatic increase in Titan cells, which are not phagocytosed and have diminished ability to directly cross biological barriers. This explains the limited dissemination of *pdr802* mutant cells to the central nervous system and the consequently reduced virulence of this strain. The role of Pdr802 as a negative regulator of Titan cell formation is thus critical for cryptococcal pathogenicity.

IMPORTANCE

The pathogenic yeast *Cryptococcus neoformans* presents a worldwide threat to human health, especially in the context of immunocompromise, and current antifungal therapy is hindered by cost, limited availability, and inadequate efficacy. After the infectious particle is inhaled, *C. neoformans* initiates a complex transcriptional program that integrates cellular responses and enables adaptation to the host lung environment. Here we describe the role of the transcription factor Pdr802 in the response to host conditions and its impact on *C. neoformans* virulence. We identified direct targets of Pdr802 and also discovered that it regulates cellular features that influence movement of this pathogen from the lung to the brain, where it causes fatal disease. These findings advance our understanding of a serious disease.

INTRODUCTION

Cryptococcosis is a fungal infection caused by *Cryptococcus neoformans* and *Cryptococcus gattii. C. neoformans* is a ubiquitous opportunistic pathogen that infects mainly immunocompromised patients, while *C. gattii* is capable of infecting immunocompetent individuals (1). Cryptococcosis causes 180,000 deaths worldwide each year, including roughly 15% of all AIDS-related deaths (2), and is initiated by the inhalation of spores or desiccated yeast cells. In immunocompetent individuals, this typically leads to an asymptomatic pulmonary infection that is controlled by the host immune response, although a population of *C. neoformans* may remain latent for extended periods of time (3–5).

44 Under conditions of immunocompromise, cryptococci disseminate from the lung to
45 the brain. Mechanisms that have been suggested to mediate fungal crossing of the
46 blood-brain barrier (BBB) include transcellular migration, in which the yeast cells enter
47 and exit vascular endothelial cells (6–9); paracellular movement, in which they cross the
48 BBB at junctions between endothelial cells (10–12); and 'Trojan horse' crossing, whereby
49 macrophages harboring *C. neoformans* enter the brain (13). Cryptococcal
50 meningoencephalitis is difficult to treat and frequently lethal, for reasons that include the
51 availability and cost of therapy (14, 15).

52 The ability of *C. neoformans* to survive and proliferate in the lung, and
53 subsequently disseminate to the brain, depends on viability at mammalian body
54 temperature and the expression of multiple virulence traits; these include secreted factors
55 (16, 17), a polysaccharide capsule that surrounds the cell wall (18), and the production of
56 giant (Titan) cells (19, 20). One secreted molecule, the pigment melanin, associates with
57 the cell wall, where its antioxidant properties protect fungal cells from reactive oxygen
58 species produced as a host immune defense (21–25). Urease, a secreted metalloenzyme
59 that converts urea to ammonia and CO_2, may affect the course of infection by modulating
60 environmental pH and damaging host tissue structure (11, 12, 26).

61 The capsule, composed primarily of large polysaccharides (27–29), is a key
62 cryptococcal virulence factor that impairs phagocytosis by immune cells (30–35). This
63 dynamic entity changes its size and structure during interactions with the host or external
64 environment (36–39), contributing to fungal adaptation (40, 41). Capsule polysaccharides
65 that are shed from the cell enable diagnosis of cryptococcal infection and also impede
66 host responses (35, 42).

67 Titan cells display a cryptococcal morphotype that has been variously
68 characterized as having cell body diameter (excluding the capsule) greater than 10 or 15
69 μm or total cell diameter (including the capsule) that exceeds 30 μm (20, 43, 44). These
70 cells are polyploid and produce normal-size cells during infection (19, 45, 46). Titan cell
71 formation is triggered by exposure to the host environment, including nutrient starvation,
72 reduced pH, and hypoxia (47–49), although the extent of induction depends on the host
73 immune response and the duration of infection (45, 50). Titan cell production appears to
74 benefit the development of pulmonary *C. neoformans* infection, since these large cells
75 are less susceptible to internalization by host phagocytes and more resistant to oxidative
76 stress than normal-size cells (19, 46). Some of these effects may be explained by the
77 highly cross-linked capsule and thickened cell wall of Titan cells (51). In contrast to their
78 success in the lungs, Titan cells show impaired dissemination to the brain (19, 46).

79 *C. neoformans* experiences a dramatic change in conditions upon entering a host,
80 including altered nutrient levels and pH. To adapt to the new environment, cryptococci
81 activate a network of transcription factors (TFs) (39, 52). For example, imbalances in ion
82 homeostasis trigger transcriptional changes mediated by the TFs Zap1 (53), Cuf1 (54),
83 Pho4 (55), Cir1 (56), and Crz1 (57). Alkaline pH stimulates expression of the TF Rim101,
84 which enables growth under basic conditions and other stresses such as high salt and
85 iron limitation; it also promotes the association of capsule polysaccharide with the cell
86 and the formation of Titan cells (47, 58).

87 Overlapping TF circuits regulate cryptococcal virulence determinants, including
88 polysaccharide capsule production and melanin synthesis. For example, Usv101, an
89 important regulator of capsule thickness and polysaccharide shedding, also regulates

90 three other TFs (Gat201, Crz1, and Rim101) and multiple polysaccharide-related
91 enzymes (59). Gat201 further regulates additional virulence-related transcription factors
92 and the anti-phagocytic protein Blp1 (60), while Crz1 plays a central role in the
93 maintenance of plasma membrane and cell wall stability (57, 61, 62). Crz1 expression is
94 also modulated by the calcineurin signaling pathway, which is required for normal yeast
95 growth at 37°C, virulence, and sexual reproduction (63). A group of TFs, including
96 Usv101, Bzp4, Hob1, and Mbs1 (59, 64), act together to regulate melanin production;
97 deletion of Bzp4 also alters capsule (52).

98 In this study, we investigated the TF Pdr802. The corresponding gene has a high
99 rate of non-synonymous mutations, which suggests it is evolving rapidly (65). Pdr802 has
100 previously been implicated in *C. neoformans* virulence (39, 52, 66), but its specific role
101 and targets are not known. We discovered that Pdr802 is induced in host-like conditions,
102 is a negative regulator of Titan cell formation, and influences capsule thickness and
103 phagocytosis by macrophages. It also regulates genes whose products act in cell wall
104 remodeling, virulence factor production, resistance to host temperature and oxidative
105 stress, and quorum sensing. These functions make Pdr802 critical for cryptococcal
106 survival in the lung and dissemination to the brain.

107

108 **RESULTS**

109 **The role of Pdr802 in *C. neoformans* virulence**

110 The importance of Pdr802 in *C. neoformans* virulence has been demonstrated in
111 multiple experimental models. Liu and collaborators first reported in 2008 that partial
112 deletion of *PDR802* reduced *C. neoformans* infectivity in a competition assay of pooled

113 *C. neoformans* strains (66). In 2015, Maier *et al* showed that a *pdr802* deletion mutant
114 had reduced virulence when tested individually in a short-term mouse model of infection
115 (39). Later that year, Jung and colleagues reported that Pdr802 was required for full
116 virulence in both wax moth larvae and short-term mouse infection using pooled strains
117 (52). Most recently, Lee and collaborators showed that Pdr802 was required for brain
118 infection (67).

119 To further investigate the role of Pdr802 in pathogenesis, we complemented a
120 complete deletion strain in the KN99α background that we had previously generated
121 (*pdr802*) (39) with the intact gene at its native locus (*PDR802*). To examine targets of
122 Pdr802, we also constructed a strain that expresses the protein fused to mCherry at its
123 N-terminus (Figure S1A). All of these strains lacked or expressed RNA encoding *PDR802*
124 or its modified forms as expected (Figure S1B) and *PDR802* was expressed at wild-type
125 levels in the complemented and modified strains (Figure S1C).

126 We next assessed the long-term survival of C57BL/6 mice infected with the
127 parental wild-type strain (KN99α), the deletion mutant (*pdr802*), or the complemented
128 mutant (*PDR802*). In this model, mice infected with the parent or complemented strains
129 survived for roughly three weeks, while those infected with the deletion mutant showed a
130 striking increase in survival: all animals survived for at least 65 days and over half
131 survived to the end of the study (100 days; Figure 1A). The lung burden measured at the
132 time of death for *pdr802*-infected mice in this study was approximately 100-fold lower
133 than that of wild type infections (Figure S2A), demonstrating the importance of this TF in
134 *C. neoformans* virulence. Mean brain burden at the time of death was more similar
135 between mutant and wild type infections (Figure S2A), although we did note some

136 heterogeneity in this measure for *pdr802*-infected mice; animals sacrificed at around two
137 months of infection (red symbols) showed brain burden similar to WT levels, while brain
138 burden of mice sacrificed at day 100 (blue symbols) ranged between zero fungal cells
139 and WT level.

140 We next examined the time course of fungal proliferation in the lungs. As
141 expected, the burdens of WT and the complemented mutant strains increased steadily
142 over an 18-day interval (Figure 1B), eventually reaching roughly 10^5 times the original
143 inoculum. Towards the end of this period, these cells were also detected in the blood and
144 brain (Figure S2B). In contrast, the lung burden of *pdr802* remained close to the inoculum
145 throughout this period, with no mutant cells detected in the blood or brain. At a late time
146 point of *pdr802* infection (75 days), we again noted some heterogeneity of fungal burden:
147 one mouse had high lung burden with no dissemination, another had high lung burden
148 with moderate brain burden, and the third had extremely low lung burden with no
149 dissemination (Figure S2C). No colony-forming units (CFU) were detected in the blood of
150 *pdr802*-infected mice at any point during infection. These results suggest that even
151 though the *pdr802* mutant is generally hypovirulent and remains at low levels in the lung,
152 it can occasionally reach the brain and, given enough time, accumulate there (see
153 Discussion).

154 Given the dramatic effects of Pdr802 on fungal virulence, we wondered about the
155 specific biological processes in which this transcription factor is involved. We first
156 examined the behavior of the *pdr802* strain *in vitro*, including stress conditions that might
157 be encountered in the host. We saw no differences in growth of the mutant compared to
158 WT cells under conditions that challenge cell or cell wall integrity, including the presence

159 of sorbitol, high salt, cell wall dyes, caffeine, sodium dodecyl sulfate (SDS), or ethanol
160 (Figure S3A-C). The mutant also showed no altered susceptibility to elements of the host
161 response, such as nitrosative or oxidative stresses, or in melanin production. All of these
162 results held whether growth was at 30°C, 37°C, or 37°C in the presence of 5% CO_2,
163 which was recently described as an independent stress for *C. neoformans* (68) (Figure
164 S3A-C). Finally, the mutant showed no difference from wild-type cells in secretion of
165 urease at 30°C or 37°C (Figure S3D).

166 **Pdr802 is regulated by "host-like" conditions**

167 We next tested the growth of the *pdr802* mutant under conditions more like those
168 encountered inside the mammalian host, using tissue culture medium (DMEM) at 37°C in
169 the presence of 5% CO_2. We found that although the *pdr802* mutant grew like WT in rich
170 medium (YPD), it grew poorly in DMEM (Figure S4A-B). To test whether the mutant cells
171 were dead or just static after growth in DMEM, we plated aliquots on solid medium to
172 measure CFU over time (Figure 2A). The *pdr802* culture showed a dramatic decrease in
173 viability compared to WT and the complemented strain, which was greatest in the first 24
174 h. This is the same time frame in which expression of the *PDR802* gene shows a striking
175 increase in wild type cells, as measured by RNA-Seq (Figure 2B).

176 Another important feature that is induced by growth in DMEM at 37°C and 5% CO_2
177 is the polysaccharide capsule, which we previously reported to be regulated by Pdr802,
178 based on negative staining with India ink (39). Fluorescence microscopy confirmed
179 increased capsule thickness of the mutant, which reverted to WT in the complemented
180 strain (Figure 3A). To quantify this change, we took advantage of a semi-automated
181 assay that we have developed (Figure S5), which measures capsules on a population

182 scale (Figure 3B) and is therefore very sensitive. This analysis showed that the capsule
183 thickness of *pdr802* cells resembles that of the well-studied hypercapsular mutant *pkr1*
184 (39, 69, 70) and is completely restored to WT by complementation at the native locus
185 (Figure 3C). Previous studies suggest that capsule thickness upon induction reflects the
186 size of the dominant capsule polymer (glucuronoxylomannan; GXM) (71, 72), which can
187 be analyzed by agarose gel migration and blotting with anti-capsule antibodies (71).
188 Consistent with the difference we observed in capsule thickness by imaging, this method
189 showed decreased mobility of GXM from *pdr802* as capsule induction progressed (Figure
190 S4C).

191 To validate the observations that we had made in standard 'host-like' conditions
192 based on synthetic tissue culture medium, we conducted similar studies in mouse serum
193 at 37°C and 5% CO_2. These conditions induced an even more pronounced hypercapsular
194 phenotype of the *pdr802* mutant (Figures 4A and 4B), as well as reduced cell viability
195 (Figure 4C) and increased cell body diameter (Figure 4D).

196 We were intrigued by the enlarged cell body and capsule of the *pdr802* mutant
197 cells in host-like conditions *in vitro* and decided to examine these phenotypes *in vivo*. For
198 these studies, we isolated fungal cells from the lungs of mice at various times after
199 infection and assessed their morphology by negative staining (Figure 5A). At each time
200 point, the mean mutant cell body diameter was larger than that of the controls.
201 Additionally, while this parameter was stable for WT and complemented strains
202 throughout the infection period, it trended larger at the end of the infection period for the
203 deletion mutant (Figure 5B). In contrast, mutant capsule thickness, although initially
204 larger than that of control cells, changed little throughout the period, while capsule

205 thickness of control cells increased to that level or beyond (Figure 5C). Furthermore,
206 although the total cell diameter of *pdr802* cells consistently exceeded that of WT and
207 complemented cells, their sizes became more comparable late in infection (Figure S6A).
208 Over time, therefore, the ratio of total cell diameter to cell body diameter for WT and
209 *PDR802* cells steadily increased, while it remained roughly constant for the mutant
210 (Figure S6B).

211 **Pdr802 negatively regulates Titan cell formation**

212 We were particularly interested in the cell size phenotype of *pdr802* because Titan
213 cells have been strongly implicated in cryptococcal pathogenesis (19). By any definition
214 of this morphotype (cell body diameter greater than 10 or 15 μm or total cell diameter
215 greater than 30 μm), our mutant cell populations were dramatically enriched in Titan cells
216 at every time of infection that we assessed (Figure S6C).

217 To specifically test Titan cell formation by the *pdr802* strain, we subjected mutant
218 cells to *in vitro* conditions that induce this process (49) and analyzed the resulting
219 population by flow cytometry. Consistent with our *in vivo* observations, Titan cells
220 constituted a much larger fraction of the population in the mutant culture (13.2%) than in
221 the WT and complemented cultures (1.62% and 1.40%, respectively) (Figure 6).

222 Titan cells are poorly engulfed by host phagocytes (19, 45, 73), which may reflect
223 their increased size as well as alterations in capsule and cell wall (51). We observed this
224 reduced uptake for all strains after growth in conditions that favor Titan cell formation
225 (Figure 7, Titan vs YPD). Also, all strains showed a reduction in phagocytosis after
226 capsule induction in DMEM (Figure 7, DMEM vs YPD), which is not surprising because

227 the capsule is antiphagocytic (31, 73). Notably, the reduction in uptake was greatest for
228 the *pdr802* mutant in both of these conditions, even though it showed normal engulfment
229 when all strains were grown in the control condition (YPD). This is likely because the
230 mutant culture is both hypercapsular and enriched in Titan cells.

231 **Identification of direct, functional targets of Pdr802**

232 To identify direct targets of Pdr802, we performed chromatin immunoprecipitation
233 followed by sequencing (ChIP-Seq). We then compared the DNA sequences
234 immunoprecipitated by anti-mCherry mAb from cells expressing mCherry-Pdr802, which
235 grow similarly to WT (Figure S7A), and untagged cells. Both strains were grown for 24
236 hours in DMEM at 37°C and 5% CO_2, as this condition induces *PDR802* expression
237 dramatically compared to standard YPD growth conditions (Figure 2B).

238 Using 2-fold-enrichment over control as a cutoff value for peaks with adjusted p
239 value <0.05, we identified 656 binding sites for mCherry-Pdr802 in genomic DNA. Of
240 these, 540 occurred within 1,000 bp upstream of transcription start sites (Data Set S1,
241 Sheets 1 and 2), which we used as an approximation of regulatory regions. Application of
242 Discriminative Regular Expression Motif Elicitation (DREME) (74) to this set of upstream
243 regions identified several putative Pdr802 binding motifs, which were highly enriched in
244 GA (TC) (Figure S7B). Notably, the ChIP-seq data also suggested self-regulation of
245 *PDR802*, as has been reported for other cryptococcal TFs (75, 76) (Figure S7C).

246 To complement our ChIP studies, we determined the set of genes regulated by
247 Pdr802 under host-like conditions by performing RNA-Seq of WT and *pdr802* cells after
248 growth for 24 h in DMEM at 37°C and 5% CO_2 (Data set 1, Sheet 3). We then used dual-

249 threshold optimization (DTO) to analyze the RNA-seq and ChIP-seq data sets together.
250 This statistical method allowed us to combine the evidence from binding and expression
251 studies to converge on a set of direct and functional TF targets (77). The Pdr802 target
252 genes yielded by this analysis include key players in multiple processes implicated in
253 cryptococcal virulence, including quorum sensing, Titan cell formation, and stress
254 resistance (Data set 1, Sheets 4 and 5).

255 **Pdr802 represses Titan cell production through regulation of quorum sensing**
256 **proteins**

257 The most striking phenotype we observed in cells lacking *PDR802* is the marked
258 increase in Titan cell formation. We therefore examined our DTO target list for genes
259 known to influence this phenotype, such as those involved in quorum sensing. Recent
260 studies have shown that the quorum sensing peptide Qsp1 is a negative regulator of
261 Titan cell formation (47, 48); Titan cell formation increases upon deletion of the gene
262 encoding this peptide (*QSP1*) or proteins that mediate its maturation and import (*PQP1*
263 and *OPT1*, respectively). We found that Pdr802 positively regulates *PQP1* and *OPT1*
264 gene expression (Table 1), consistent with its repression of Titan cell formation.

265 A study of *C. neoformans* cells exposed to Titan cell inducing conditions *in vitro*
266 reported that 562 genes were upregulated in this condition, while 421 genes were
267 downregulated (48). The overlap of these genes with our DTO set of Pdr802-regulated
268 genes included three TF genes *LIV3*, *STB4*, and *ZFC3* (48) (Data Set S2, Sheets 1 and
269 2). The first two are repressed during Titan cell induction while *ZFC3* (also known as
270 *CQS2*) is induced. Our analysis showed that Pdr802 positively regulates expression of
271 *LIV3* and *STB4*, while it negatively regulates *ZFC3* (Table 1), in concordance with our

272 phenotypic observations of Titan cell formation. Notably, Liv3 and Zfc3 are responsive to
273 the peptide Qsp1 (75, 76) and are important for *C. neoformans* virulence, while Stb4
274 influences cryptococcal brain infection (67).

275 **Pdr802 coordinates cryptococcal response to the host environment**

276 *C. neoformans* deploys a variety of proteins to resist the many challenges it
277 experiences upon host entry, which include oxidative and temperature stress. Multiple
278 genes that are central to these responses were identified as direct, functional targets of
279 Pdr802 by our DTO analysis (Table 2). For example, Pdr802 induces the expression of
280 genes whose products detoxify reactive oxygen species (ROS), such as *CAT1*, *CAT2*,
281 and *SOD1* (78, 79), or participate in resistance to these compounds, such as *FZC34*,
282 *MIG1*, and *CCK1* (52, 80, 81) (Table 2). Both the kinase Cck1 (also known as Yck2) and
283 the TF Fzc34 have been implicated in cryptococcal virulence (80, 82).

284 As noted above, melanin has important anti-oxidant properties that promote
285 cryptococcal survival inside the host (16). Under host-like conditions, Pdr802 regulates
286 genes required for melanization, even though it melanizes normally *in vitro*. These genes
287 include *CAC1*, *PKC1*, *CUF1*, and *SNF5* (Table 2). Cac1 is an adenylyl cyclase
288 responsible for cyclic AMP (cAMP) production in *C. neoformans*, which plays a central
289 role in melanin synthesis as well as proper capsule production, mating and virulence (83).
290 The kinase Pkc1 induces production of the laccase (Lac1) that forms melanin and plays a
291 key role in resistance to oxidative and nitrosative stress (84, 85); the TF Cuf1 regulates
292 *LAC1* expression and is important for cryptococcal virulence (86, 87); and *SNF5* is
293 required for full melanization (88). Melanin occurs in the fungal cell wall, which is another
294 key component in fungal stress resistance. Pdr802 is also a direct, functional regulator of

295 several genes whose products influence cell wall glycan content: two chitin deacetylases
296 (Cda3 and Mp98) and the mannoprotein MP88 (Table 2). Changes in mannose and chitin
297 occur in Titan cell walls (51).

298 Pdr802 positively regulates the expression of several proteins required for yeast
299 growth at 37ºC, including the kinases Kic1 and Ire1 (Table 2). Ire1 is a regulator of the
300 cryptococcal Unfolded Protein Response (UPR) pathway and lack of Ire1 or Kic1 impacts
301 *C. neoformans* virulence (80, 89). Pdr802 also modulates cryptococcal urease activity,
302 which is required for dissemination to the central nervous system (CNS) (11, 12), by
303 regulating the urea transporter Dur3 and other proteins that influence urease activity (e.g.
304 the kinases Fab1, Kin1, and Gut1 and the TF Hlh1) (Table 2). Deletion of *FAB1*, *KIN1*, or
305 *HLH1* impair urease activity in *C. neoformans*, while *GUT1* disruption induces it (52, 80).

306 Above we documented the role of Pdr802 in capsule synthesis, which is
307 dramatically upregulated in the host environment in general and is further increased in
308 cells lacking this TF. We found that Pdr802 is a positive regulator of multiple genes that
309 have been implicated in reducing cryptococcal capsule thickness. These include the
310 kinases Arg2, Iks1, and Ksp1; the TF Fzc51; and the phosphodiesterase Pde2 (Table 2).
311 Notably, null mutants for those genes are hypercapsular, similar to *pdr802* cells (52, 80,
312 90). Pdr802 is a negative regulator of the TF Bzp4, which, as mentioned above, positively
313 regulates capsule (Table 2) (52).

314 **Pdr802 regulates calcineurin target genes**

315 The calcineurin signaling pathway is activated by calcium and governs stress
316 response and virulence in *C. neoformans* (91–93). One major mediator of calcineurin

317 signaling is the transcription factor Crz1 mentioned above, which is highly responsive to
318 temperature and influences cryptococcal virulence (57, 62). Upon intracellular calcium
319 influx calcineurin dephosphorylates Crz1, which then translocates to the nucleus and
320 regulates gene expression (57, 63). We found that Pdr802 binds the *CRZ1* gene
321 promoter and positively regulates its expression (Figure 8A, Table 2, and Data Set S2,
322 Sheet 3). Pdr802 also binds and regulates five other genes whose products are
323 dephosphorylated by calcineurin; these include the phosphatase Had1, which is
324 important for cryptococcal cell wall remodeling and virulence (Figure 8B, Table 2, and
325 Data Set S2, Sheet 3) (63, 94).

326 Because Crz1 helps maintain normal cryptococcal Ca^{2+} concentrations through the
327 regulation of calcium transporters (57), we wondered about the intracellular calcium
328 levels in *pdr802* cells. We found that after 24 hours of growth in DMEM, the level of
329 cytosolic calcium in the mutant significantly exceeded that of WT or complemented
330 strains (Figure 8C). It was still, however, below that of a *crz1* null mutant, supporting that
331 Pdr802 is not the sole regulator of *CRZ1* expression. Notably, *PDR802* deletion had no
332 effect in rich medium (YPD), which reinforces our hypothesis that Pdr802 acts primarily in
333 host-like conditions. To further explore the relationship of Pdr802 and calcineurin, we
334 compared published gene expression profiles of a calcineurin mutant (57) to our DTO
335 data set. Of the 393 genes that are differently expressed in the calcineurin mutant under
336 thermal stress, 26 are regulated by Pdr802 (Data Set S2, Sheet 4).

337

338 **DISCUSSION**

339 We have shown that Pdr802 is a potent regulator of cryptococcal responses to the
340 host environment. In this context, it influences the formation of capsule and Titan cells as
341 well as cellular responses to temperature and oxidative stress, acts as a downstream
342 effector of calcineurin, and modulates calcium availability. The last function is likely
343 achieved through its positive regulation of the transcription factor Crz1, which in turn
344 modulates the calcium transporters Pmc1 and Vcx1 (57). Since calcium ion is a major
345 second messenger in eukaryotic cells, its accumulation in *pdr802* cells affects multiple
346 processes central to host interactions, including stress responses, cell wall integrity, and
347 capsule size (61, 62, 92, 95, 96).

348 *C. neoformans* dissemination to the brain is the main driver of patient mortality (2).
349 We found that dissemination of *pdr802* cells is significantly impaired, although they do
350 occasionally reach the brain. These observations can be explained by a combination of
351 factors. First, the limited accumulation of the *pdr802* mutant in the lungs, due to factors
352 summarized above, may directly affect dissemination (97). Second, this strain survives
353 poorly in mouse serum, as demonstrated directly by our culture experiments and
354 indirectly by our inability to detect it in the blood of infected mice, even 75 days after
355 infection. The latter might be because the cells do not reach the blood or because they
356 are rapidly eliminated, consistent with previous observations (98). Third, the thick
357 capsules of the *pdr802* mutant reduce its ability to reach the brain. This is true whether
358 fungal entry occurs directly, by the movement of free fungi across the BBB, or indirectly,
359 via a Trojan horse mechanism that requires macrophage uptake (99); such uptake is
360 impeded by enlarged capsules, independent of cell size (31). Fourth, calcium imbalance
361 directly affects cryptococcal transmigration (100). Finally, *pdr802* cells show reduced
362 expression of genes required for urease activity, which promotes *C. neoformans*

363 dissemination to the CNS (11, 12, 100). Interestingly, despite all of these obstacles to
364 dissemination, mutant cells that do reach the brain are able to proliferate to wild-type
365 levels.

366 Titan cells are a robust and persistent morphotype of *C. neoformans* that
367 contributes to yeast virulence (45). We showed that cells lacking Pdr802 demonstrate
368 increased formation of Titan cells *in vivo* and *in vitro*, suggesting that this TF is a novel
369 repressor of this process. Although Titan cells enhance aspects of cryptococcal
370 pathogenesis (19, 101), their overproduction negatively impacts dissemination to the
371 brain due to their resistance to phagocytosis by macrophages (19, 45) and decreased
372 penetration of biological barriers (19).

373 Our combined analysis of DNA binding and gene expression data allows us to
374 understand the increase in Titan cell formation that occurs upon deletion of *PDR802*.
375 Under host-like conditions, Pdr802 positively regulates Pqp1, Opt1 and Liv3, all key
376 proteins in the cryptococcal quorum sensing pathway, which represses Titan cell
377 formation (47, 48). In the absence of this TF, quorum sensing is impaired, increasing
378 Titan cell formation. Pdr802 may also indirectly modulate Titan cell formation by
379 regulating other TFs that impact this process, such as Zfc3 (Cqs2) and Stb4.

380 We know that capsule, a key virulence factor, is typically highly induced in the host
381 or host-like conditions (102). Our studies *in vitro*, *ex vivo*, and *in vivo* show that Pdr802
382 normally reins in this process. This likely occurs via a combination of Pdr802's repression
383 of the TF Bzp4, which positively regulates capsule size, and the induction of other factors
384 (e.g. the TF Fzc1, the phosphodiesterase Pde2, and the kinases Ksp1, Arg2, and Iks1)
385 that negatively regulate capsule size (52, 80, 90).

386 Overall, we found that Pdr802 influences key cryptococcal phenotypes that
387 influence virulence, including quorum sensing, stress responses, Titan cell formation, and
388 capsule production (Figure 9). We have further identified multiple genes that are central
389 in these processes and are directly regulated by Pdr802. Some of these targets are also
390 regulated by calcineurin (e.g. Had1 and Crz1) or by another important TF, Gat201 (e.g.
391 Opt1, Liv3, Zfc3) (60, 75, 76). Finally, the expression of *PDR802* itself is regulated by the
392 TFs Gat201 and Hob1 (67, 76). The crosstalk between all of these regulatory
393 mechanisms remains to be dissected. Nonetheless, it is evident that Pdr802 is critical for
394 both survival in the lung and dissemination to the brain, thus explaining its role in
395 cryptococcal virulence.

396

397 **MATERIALS AND METHODS**

398 **Strain construction and cell growth**

399 We previously reported the *PDR802* deletion mutant (*pdr802*) in the KN99α strain
400 background (103) that was used in this work (39). Complementation of this mutant with
401 the wild-type gene at the native locus (*PDR802*) and construction of a strain that
402 expresses Pdr802 with N-terminal mCherry (mCherry-Pdr802) are detailed in the
403 Supplementary Methods. For all studies, *C. neoformans* strains were inoculated from
404 single colonies into YPD medium (2% [wt/vol] dextrose, 2% [wt/vol] Bacto peptone and
405 1% [wt/vol] yeast extract in double-distilled water [ddH_2O]) and grown overnight at 30°C
406 with shaking at 230 rpm before further handling as detailed below. To assess viability
407 during growth in tissue culture medium, overnight cultures were washed with phosphate-
408 buffered saline (PBS), diluted to 10^6 cells/ml in DMEM (Sigma, D6429), plated (1 ml/well)

409 in triplicate in 24-well plates, and incubated at 37°C and 5% CO_2. At the indicated times
410 cells were mixed thoroughly, diluted in PBS, and plated on YPD agar (YPD medium, 2%
411 agar [wt/vol]) for assessment of colony-forming units (CFU). To assess viability during
412 growth in mouse serum (prepared as below), YPD-grown cryptococcal cells (10^3) were
413 incubated in 100 µl of serum in 96-well plates for 24 h at 37°C and 5% CO_2 and CFU
414 assessed as above.

415 **Animal experiments**

416 All animal protocols were approved by the Washington University Institutional Animal
417 Care and Use Committee (reference 20170131) or Comissão de Ética no Uso de
418 Animais – CEUA (reference 30936), and care was taken to minimize handling and
419 discomfort. For survival studies, groups of five 4- to 6-week-old female C57BL/6 mice
420 (The Jackson Laboratory) were anesthetized by subcutaneous injection of 1.20 mg
421 ketamine and 0.24 mg xylazine in 120 µl sterile water and intranasally infected with 5 x
422 10^4 cryptococcal cells. The mice were monitored and humanely sacrificed when their
423 weight decreased to below 80% of initial weight or if they showed signs of disease, at
424 which point organ burden was assessed. The lungs and brains were harvested,
425 homogenized, diluted and plated on YPD agar. The resulting CFU were enumerated and
426 survival differences were assessed by Kaplan-Meier analysis.

427 For timed organ burden studies, *C. neoformans* overnight cultures were centrifuged
428 (1,000 x *g* for 3 min), washed with sterile PBS, and resuspended in PBS to 1 x 10^6
429 cells/ml. Groups of three 4- to 6-week-old female C57BL/6 mice (Centro Multidisciplinar
430 para Investigação Biológica na Área da Ciência em Animais de Laboratório, CEMIB)
431 were anesthetized as above and intranasally infected with 5 x 10^4 cryptococcal cells, and

432 monitored as above. At set time points post-infection (see text), mice were sacrificed and
433 fungal burden was assessed from organs (as above) or blood (obtained by cardiac
434 puncture). Organ burden was analyzed by Kruskal-Wallis test with Dunn's multiple
435 comparison *post hoc* test for each day post-infection.

436 To assess cryptococcal viability in mouse serum, 6 BALB/c mice were anesthetized with
437 isoflurane and blood was collected from the retro-orbital space using a sterile capillary
438 tube. Collected blood was incubated at 37°C for 30 min and serum was isolated by
439 centrifugation at 1,000 x *g* for 15 min and then heat-inactivated at 56 °C for 30 min.

440 **Capsule analysis**

441 To qualitatively assess capsule thickness, strains were grown in YPD medium for 16 h,
442 washed with PBS, and 10^6 cells were incubated in DMEM or mouse serum for 24 h at
443 37°C and 5% CO_2. After incubation, cells were fixed in 4% paraformaldehyde, washed
444 three times with PBS, and mixed with similar volumes of India ink for capsule
445 visualization and measurement as previously described (104).

446 For population-level capsule measurement, *C. neoformans* strains were grown overnight
447 in YPD, washed with PBS, and diluted to 10^6 cells/ml in DMEM. 150 µl aliquots were then
448 plated in quadruplicate in a poly-L-lysine coated 96-well plate (Fisher 655936) and
449 incubated at 37°C and 5% CO_2. After 24 hours, the cells were washed with PBS and
450 incubated with 150 µl of a staining mixture (100 µg/ml Calcofluor white to stain cell walls,
451 50 µg/ml of anticapsular monoclonal antibody 302 conjugated to Alexa Fluor 488
452 (Molecular probes), and 1.5% goat serum in PBS) for 30 minutes at room temperature in
453 the dark. The cells were washed again with PBS, fixed with 4% formaldehyde for 10
454 minutes at room temperature, washed with PBS, and each well refilled with 150 µl PBS.

455 The cells were imaged using a BioTek Cytation 3 imager, which automatically collected
456 100 images per well in a grid pattern at the well center. Image files were prepared for
457 analysis with the GE InCell Translator and assembled into .xdce image stacks for
458 analysis with the GE INCell Developer Toolbox 1.9. Cell wall and capsule images were
459 first filtered to remove background noise and border objects and then cells were identified
460 using shape-based object segmentation (3-pixel kernel, 50% sensitivity) followed by
461 watershed clump breaking to prevent apparent connectivity caused by incomplete
462 segmentation. Target linking was performed to assign each cell wall object to one
463 capsule object based on known 1:1 pairing and location, generating a target set. Capsule
464 and cell wall object diameters were calculated for each target set (hundreds to thousands
465 per well), and the difference between each pair of measurements was defined as the
466 capsule thickness. Data were normalized by the difference in capsule thickness between
467 uninduced and induced WT cells, which were included in each experiment, and
468 compared to hypercapsular (*pkr1*) (39) and hypocapsular (*ada2*) (105) control strains in
469 each experiment. Capsule sizes were compared by One-Way ANOVA with Dunnett's
470 multiple comparison *post hoc* test.

471 To measure capsule thickness of cryptococcal cells grown in the lungs of infected mice,
472 lung homogenates were filtered through a cell strainer with 40 μm pores using a syringe
473 plunger, fixed in 3.7% formaldehyde, and used for India ink staining and measurement as
474 above. For the visualization of KN99α and *PDR802* cells from mouse lungs after 18 days
475 of infection, the tissue was treated with 50 μg/ml DNAse I for 30 min at 37°C.

476 GXM immunoblotting was conducted as previously described (71). Briefly, 10^6 cells/ml
477 were grown in DMEM for 24 and 48h. Culture supernatant fractions were then resolved

478 by gel electrophoresis on 0.6% agarose, transferred onto nylon membranes, and probed
479 with 1 µg/ml anti-GXM antibody 302.

480 **Phenotypic assays**

481 For stress plates, cryptococcal cells were grown overnight in YPD, washed with PBS, and
482 diluted to 10^7 cells/ml in PBS. Aliquots (3 µl) of 10-fold serial dilutions were spotted on
483 YPD or YNB agar supplemented with various stressors (sorbitol, NaCl, $CaCl_2$, LiCl,
484 Congo Red, Calcofluor white, caffeine, SDS, $NaNO_2$, H_2O_2 and ethanol) in the
485 concentrations indicated in the figures. Melanization was tested on plates made by
486 mixing 10 ml of 2X minimal medium (2 g/L L-asparagine, 1 g/L $MgSO_4 \cdot 7H_2O$, 6 g/L
487 KH_2PO_4, 2 g/L thiamine, 2 mM L-3,4-dihydroxyphenylalanine [L-DOPA] and 0.1%
488 dextrose was added for melanization induction or 0.5% for melanization inhibition) with
489 10 ml of 2% agar-water per plate. A control strain lacking the ability to melanize was used
490 as a control (*lac1*) (88). For the solid urease assay, 10 µl of a 10^7 cells/ml suspension in
491 water was plated on Christensen's urea solid media (1 g/L peptone, 1 g/L dextrose, 5 g/L
492 NaCl, 0.8 g/L KH_2PO_4, 1.2 g/L Na_2HPO_4, 0.012 g/L phenol red and 15 g/L agar, pH 6.8).
493 Plates were incubated at 30°C or 37°C.

494 **Titan cells**

495 Titan cell induction was performed in 1x PBS supplemented with 10% heat inactivated
496 Fetal Calf Serum (FCS) for 72 hours at 37°C and 5% CO_2 as recently described (49) and
497 quantified by flow cytometry as previously reported (47, 48).

498 **Phagocytosis**

499 J774.16 cells were prepared for uptake experiments by seeding (10^5 cells/well) in a 96-
500 well plate and incubating in DMEM supplemented with 10% Fetal Bovine Serum (FBS) at
501 37°C and 5% CO_2 for 24 h. *C. neoformans* cells were prepared for uptake experiments
502 by inoculating an overnight culture in YPD into either DMEM or Titan cell induction
503 medium (49) and growing at 37°C and 5% CO_2 for 24 or 72 h, respectively. To initiate the
504 study, cryptococcal cells were washed with PBS and opsonized with anti-capsular
505 antibody 18B7 (1 µg/ml) for 1 h at 37°C while macrophages were activated with 50 nM
506 phorbol myristate acetate (PMA) for 1 h at 37°C and 5% CO_2; 10^6 cryptococcal cells were
507 then incubated with the macrophages for 2 h at 37°C and 5% CO_2. The wells were then
508 washed three times with warm PBS and the macrophages lysed with 0.1% Triton in PBS
509 and plated for CFU as above. Fold-change in CFU was assessed by comparison to the
510 CFU of opsonized cells. One-Way ANOVA with Dunnett's multiple comparison *post hoc*
511 test was used to compare phagocytosis of *pdr802* and *PDR802* strains with that of
512 KN99α.

513 **Chromatin Immunoprecipitation (ChIP)**

514 ChIP studies were performed as previously described (39, 105). Briefly, wild type and N-
515 terminal-mCherry-Pdr802 strains were cultivated in DMEM for 24 hours at 37°C and 5%
516 CO_2. The cells were then fixed with formaldehyde, lysed by mechanical bead-beating,
517 and the cell debris removed by centrifugation. The supernatant fraction was sheared by
518 sonication, centrifuged, and an aliquot was reserved as 'Input'. The remaining material
519 was incubated with rabbit IgG anti-mCherry antibody (Abcam, ab213511) tethered to
520 protein A sepharose ('IP') or sepharose alone ('Mock') overnight at 4°C. The beads were
521 then washed, incubated at 65°C to reverse DNA-DNA and DNA-protein crosslinks and

522 the DNA recovered by phenol/chloroform/isoamyl alcohol (25:24:1) extraction, ethanol
523 precipitation, and resuspension in nuclease-free water.

524 Samples were submitted to the Washington University Genome Technology Access
525 Center for library preparation and DNA samples were sequenced using the Illumina
526 Nextseq platform. The first replicate was sequenced using paired-end 2x75-bp reads and
527 replicates 2 and 3 were sequenced using single-end 75-bp reads; the minimum coverage
528 obtained was ~16x. The quality of the reads was evaluated by FastQC (106). Fastq files
529 were aligned to the KN99 genome (107) using NextGenMap 0.5.3 (108). SAM files were
530 converted to bam, reads were sorted and indexed, and read duplicates were removed
531 from the final bam files using samtools (109). Samtools was also used to filter out reads
532 with a mapping quality lesser than 20 phreds to guarantee single alignment of the reads.
533 Peaks were called using MACS2 (2.1.1.20160309) (110), filtered by size (maximum
534 threshold 5 kb and no minimum), and annotated using Homer 4.8 (111). The significant
535 peaks were chosen using the cutoff of fold enrichment above 2 and adjusted p value <
536 0.05 and read coverage of each peak was obtained using Samtools (109). Pdr802
537 binding motifs were identified using DREME (74); partial motifs were defined as at least 5
538 consecutive bp of the motif.

539 **RNA-Seq and Dual-Threshold Optimization (DTO)**

540 RNA from wild-type and *pdr802* cells grown for 24 hours in DMEM (37°C, 5% CO_2) was
541 isolated and sequenced as previously described (39). Briefly, cDNA samples were
542 sequenced using the Illumina Nextseq platform for single-end 1 x 75 bp reads and read
543 quality was evaluated by FastQC (106). Fastq files were aligned to the KN99 genome
544 (107) using Novoalign (112), SAM files were converted to bam, reads were sorted and

545 indexed, and read duplicates were removed from the final bam files using Samtools
546 (109). The number of reads mapped per gene was calculated using HTSeq (113) and
547 differential gene expression was analyzed with DESeq2 (114), using the Independent
548 Hypothesis Weighting (IHW) package to calculate the adjusted p-values (115). Dual-
549 Threshold Optimization (DTO) analysis was performed as recently described (77). This is
550 a method for simultaneously finding the best thresholds for significance in a TF binding
551 location dataset (e.g. ChIP) and a TF perturbation-response dataset (e.g. RNA-Seq of a
552 TF mutant). It works by trying out all pairs of thresholds for the two datasets, picking the
553 pair that minimizes the probability of the overlap between the bound and responsive gene
554 sets occurring by chance under a null model, and testing the significance of the overlap
555 by comparison to randomly permuted data. Our application of DTO to our ChIP and RNA-
556 Seq data yielded 1455 bound genes, 5186 responsive genes, and 1167 genes that were
557 both bound and responsive. Based on DTO, Pdr802 has an acceptable convergence
558 from binding and perturbation, with p value < 0.01 from the random permutation test and
559 minimum expected FDR less than or equal to 20% at 80% sensitivity. In addition to
560 requiring a statistically significant overlap between the ChIP-Seq and RNA-Seq gene
561 sets, we filtered out any genes for which traditional differential expression analysis
562 yielded an adjusted p-value ≤ 0.15 or absolute $\log_2$ of fold change ≥ 0.3, leaving 380
563 bound targets.

564 **Intracellular calcium measurement**

565 To measure intracellular free Ca^{2+}, yeast cells were cultured overnight in YPD at 30°C
566 with shaking, washed three times with deionized water, diluted to 10^6 cells/ml in DMEM
567 (Sigma, D6429), plated (1 ml/well) in triplicate in 24-well plates, and incubated at 37°C

568 and 5% CO_2 for 24 hours. At the indicated times, cells were mixed thoroughly, diluted in
569 PBS containing 2 μM Fluo4-AM (Thermo Fisher), incubated at 30°C for 30 min, and
570 analyzed using flow cytometry. The overnight culture was used as a control and treated
571 as above.

572 **Data availability**

573 ChIP-seq and RNA-seq data files are available at the NCBI Gene Expression Omnibus
574 under accession numbers GSE153134 and GSE162851, respectively.

575

576 **REFERENCES**

577 1. Kwon-Chung KJ, Fraser JA, Doering TL, Wang ZA, Janbon G, Idnurm A, Bahn Y-
578 S. 2014. *Cryptococcus neoformans* and *Cryptococcus gattii*, the Etiologic Agents of
579 Cryptococcosis. Cold Spring Harb Perspect Med 4:a019760.

580 2. Rajasingham R, Smith RM, Park BJ, Jarvis JN, Govender NP, Chiller TM, Denning
581 DW, Loyse A, Boulware DR. 2017. Global burden of disease of HIV-associated
582 cryptococcal meningitis: an updated analysis. Lancet Infect Dis 17:873–881.

583 3. Ballou ER, Johnston SA. 2017. The cause and effect of *Cryptococcus* interactions
584 with the host. Curr Opin Microbiol 40:88–94.

585 4. Sabiiti W, May RC. 2012. Mechanisms of infection by the human fungal pathogen
586 *Cryptococcus neoformans*. Future Microbiol 7:1297–1313.

587 5. Garcia-Hermoso D, Janbon G, Dromer F. 1999. Epidemiological evidence for
588 dormant *Cryptococcus neoformans* infection. J Clin Microbiol 37:3204–3209.

589 6. Chang YC, Stins MF, McCaffery MJ, Miller GF, Pare DR, Dam T, Paul-Satyasee M,
590 Kim KS, Kwon-Chung KJ. 2004. Cryptococcal yeast cells invade the central
591 nervous system via transcellular penetration of the blood-brain barrier. Infect
592 Immun 72:4985–4995.

593 7. Huang S-H, Long M, Wu C-H, Kwon-Chung KJ, Chang YC, Chi F, Lee S, Jong A.
594 2011. Invasion of *Cryptococcus neoformans* into Human Brain Microvascular
595 Endothelial Cells Is Mediated through the Lipid Rafts-Endocytic Pathway via the
596 Dual Specificity Tyrosine Phosphorylation-regulated Kinase 3 (DYRK3). J Biol
597 Chem 286:34761–34769.

598 8. Jong A, Wu C-H, Shackleford GM, Kwon-Chung KJ, Chang YC, Chen H-M,
599 Ouyang Y, Huang S-H. 2008. Involvement of human CD44 during *Cryptococcus*
600 *neoformans* infection of brain microvascular endothelial cells. Cell Microbiol
601 10:1313–1326.

602 9. Maruvada R, Zhu L, Pearce D, Zheng Y, Perfect J, Kwon-Chung KJ, Kim KS. 2012.
603 *Cryptococcus neoformans* phospholipase B1 activates host cell Rac1 for traversal
604 across the blood-brain barrier. Cell Microbiol 14:1544–1553.

605 10. Chen SHM, Stins MF, Huang S-H, Chen YH, Kwon-Chung KJ, Chang Y, Kim KS,
606 Suzuki K, Jong AY. 2003. *Cryptococcus neoformans* induces alterations in the
607 cytoskeleton of human brain microvascular endothelial cells. J Med Microbiol
608 52:961–970.

609 11. Olszewski MA, Noverr MC, Chen G-H, Toews GB, Cox GM, Perfect JR, Huffnagle
610 GB. 2004. Urease Expression by *Cryptococcus neoformans* Promotes
611 Microvascular Sequestration, Thereby Enhancing Central Nervous System

612 Invasion. Am J Pathol 164:1761–1771.

613 12. Shi M, Li SS, Zheng C, Jones GJ, Kim KS, Zhou H, Kubes P, Mody CH. 2010.
614 Real-time imaging of trapping and urease-dependent transmigration of
615 *Cryptococcus neoformans* in mouse brain. J Clin Invest 120:1683–1693.

616 13. Santiago-Tirado FH, Onken MD, Cooper JA, Klein RS, Doering TL. 2017. Trojan
617 Horse Transit Contributes to Blood-Brain Barrier Crossing of a Eukaryotic
618 Pathogen. MBio 8:e02183-16.

619 14. Jarvis JN, Bicanic T, Loyse A, Namarika D, Jackson A, Nussbaum JC, Longley N,
620 Muzoora C, Phulusa J, Taseera K, Kanyembe C, Wilson D, Hosseinipour MC,
621 Brouwer AE, Limmathurotsakul D, White N, van der Horst C, Wood R, Meintjes G,
622 Bradley J, Jaffar S, Harrison T. 2014. Determinants of Mortality in a Combined
623 Cohort of 501 Patients With HIV-Associated Cryptococcal Meningitis: Implications
624 for Improving Outcomes. Clin Infect Dis 58:736–745.

625 15. John R. Perfect, William E. Dismukes, Francoise Dromer, David L. Goldman, John
626 R. Graybill, Richard J. Hamill, Thomas S. Harrison, Robert A. Larsen, Olivier
627 Lortholary, Minh-Hong Nguyen, Peter G. Pappas, William G. Powderly, Nina Singh,
628 Jack D. Sobel TCS. 2010. Clinical Practice Guidelines for the Management of
629 Cryptococcal Disease: 2010 Update by the Infectious Diseases Society of America.
630 Chinese J Infect Chemother 50:291–322.

631 16. Nosanchuk JD, Casadevall A. 2003. The contribution of melanin to microbial
632 pathogenesis. Cell Microbiol 5:203–223.

633 17. Singh A, Panting RJ, Varma A, Saijo T, Waldron KJ, Jong A, Ngamskulrungroj P,

634 Chang YC, Rutherford JC, Kwon-Chung KJ. 2013. Factors Required for Activation
635 of Urease as a Virulence Determinant in *Cryptococcus neoformans*. MBio
636 4:e00220-13.

637 18. Chang YC, Kwon-Chung KJ. 1994. Complementation of a capsule-deficient
638 mutation of *Cryptococcus neoformans* restores its virulence. Mol Cell Biol 14:4912–
639 4919.

640 19. Okagaki LH, Strain AK, Nielsen JN, Charlier C, Baltes NJ, Chrétien F, Heitman J,
641 Dromer F, Nielsen K. 2010. Cryptococcal Cell Morphology Affects Host Cell
642 Interactions and Pathogenicity. PLoS Pathog 6:e1000953.

643 20. Zaragoza O, Nielsen K. 2013. Titan cells in *Cryptococcus neoformans*: cells with a
644 giant impact. Curr Opin Microbiol 16:409–413.

645 21. Wang Y, Aisen P, Casadevall A. 1995. *Cryptococcus neoformans* melanin and
646 virulence: Mechanism of action. Infect Immun 63:3131–3136.

647 22. Mednick AJ, Nosanchuk JD, Casadevall A. 2005. Melanization of *Cryptococcus*
648 *neoformans* Affects Lung Inflammatory Responses during Cryptococcal Infection.
649 Infect Immun 73:2012–2019.

650 23. Wang Y, Casadevall A. 1994. Susceptibility of melanized and nonmelanized
651 *Cryptococcus neoformans* to nitrogen- and oxygen-derived oxidants. Infect Immun
652 62:3004–7.

653 24. Doering TL, Nosanchuk JD, Roberts WK, Casadevall A. 1999. Melanin as a
654 potential cryptococcal defence against microbicidal proteins. Med Mycol 37:175–
655 81.

656 25. Agustinho DP, Nosanchuk JD. 2017. Functions of Fungal MelaninsReference
657 Module in Life Sciences. Elsevier.

658 26. Cox GM, Mukherjee J, Cole GT, Casadevall A, Perfect JR. 2000. Urease as a
659 virulence factor in experimental cryptococcosis. Infect Immun 68:443–8.

660 27. Bose I, Reese AJ, Ory JJ, Janbon G, Doering TL. 2003. A Yeast under Cover: the
661 Capsule of *Cryptococcus neoformans*. Eukaryot Cell 2:655–663.

662 28. Wang ZA, Li LX, Doering TL. 2018. Unraveling synthesis of the cryptococcal cell
663 wall and capsule. Glycobiology 28:719–730.

664 29. Agustinho DP, Miller LC, Li LX, Doering TL. 2018. Peeling the onion: the outer
665 layers of *Cryptococcus neoformans*. Mem Inst Oswaldo Cruz 113:e180040.

666 30. Bulmer GS, Sans MD. 1967. *Cryptococcus neoformans*. II. Phagocytosis by human
667 leukocytes. J Bacteriol 94:1480–3.

668 31. Bulmer GS, Sans MD. 1968. *Cryptococcus neoformans*. 3. Inhibition of
669 phagocytosis. 95:5–8.

670 32. Tacker JR, Farhi F, Bulmer GS. 1972. Intracellular fate of *Cryptococcus*
671 *neoformans*. Infect Immun 6:162–7.

672 33. Monari C, Bistoni F, Vecchiarelli A. 2006. Glucuronoxylomannan exhibits potent
673 immunosuppressive properties. FEMS Yeast Res 6:537–542.

674 34. Hayes JB, Sircy LM, Heusinkveld LE, Ding W, Leander RN, McClelland EE, Nelson
675 DE. 2016. Modulation of Macrophage Inflammatory Nuclear Factor κB (NF-κB)
676 Signaling by Intracellular *Cryptococcus neoformans*. J Biol Chem 291:15614–

677 15627.

678 35. Fonseca FL, Nohara LL, Cordero RJB, Frases S, Casadevall A, Almeida IC,
679 Nimrichter L, Rodrigues ML. 2010. Immunomodulatory Effects of Serotype B
680 Glucuronoxylomannan from *Cryptococcus gattii* Correlate with Polysaccharide
681 Diameter. Infect Immun 78:3861–3870.

682 36. Garcia-Hermoso D, Dromer F, Janbon G. 2004. *Cryptococcus neoformans* Capsule
683 Structure Evolution *In Vitro* and during Murine Infection. Infect Immun 72:3359–
684 3365.

685 37. Guimarães AJ, Frases S, Cordero RJB, Nimrichter L, Casadevall A, Nosanchuk
686 JD. 2010. *Cryptococcus neoformans* responds to mannitol by increasing capsule
687 size *in vitro* and *in vivo*. Cell Microbiol 12:740–753.

688 38. Cordero RJB, Pontes B, Guimarães AJ, Martinez LR, Rivera J, Fries BC,
689 Nimrichter L, Rodrigues ML, Viana NB, Casadevall A. 2011. Chronological Aging Is
690 Associated with Biophysical and Chemical Changes in the Capsule of
691 *Cryptococcus neoformans*. Infect Immun 79:4990–5000.

692 39. Maier EJ, Haynes BC, Gish SR, Wang ZA, Skowyra ML, Marulli AL, Doering TL,
693 Brent MR. 2015. Model-driven mapping of transcriptional networks reveals the
694 circuitry and dynamics of virulence regulation. Genome Res 25:690–700.

695 40. Santos JRA, Holanda RA, Frases S, Bravim M, Araujo GDS, Santos PC, Costa
696 MC, Ribeiro MJA, Ferreira GF, Baltazar LM, Miranda AS, Oliveira DB, Santos
697 CMA, Fontes ACL, Gouveia LF, Resende-Stoianoff MA, Abrahão JS, Teixeira AL,
698 Paixão TA, Souza DG, Santos DA. 2014. Fluconazole Alters the Polysaccharide

699 Capsule of *Cryptococcus gattii* and Leads to Distinct Behaviors in Murine
700 Cryptococcosis. PLoS One 9:e112669.

701 41. Silveira CP, Piffer AC, Kmetzsch L, Fonseca FL, Soares DA, Staats CC, Rodrigues
702 ML, Schrank A, Vainstein MH. 2013. The heat shock protein (Hsp) 70 of
703 *Cryptococcus neoformans* is associated with the fungal cell surface and influences
704 the interaction between yeast and host cells. Fungal Genet Biol 60:53–63.

705 42. Alspaugh JA. 2015. Virulence mechanisms and *Cryptococcus neoformans*
706 pathogenesis. Fungal Genet Biol 78:55–58.

707 43. García-Rodas R, de Oliveira H, Trevijano-Contador N, Zaragoza O. 2018.
708 Cryptococcal Titan Cells: When Yeast Cells Are All Grown up, p. 101–120. *In*
709 Current Topics in Microbiology and Immunology. Springer Verlag.

710 44. Zhou X, Ballou ER. 2018. The *Cryptococcus neoformans* Titan Cell: From *In Vivo*
711 Phenomenon to *In Vitro* Model. Curr Clin Microbiol Reports 5:252–260.

712 45. Zaragoza O, García-Rodas R, Nosanchuk JD, Cuenca-Estrella M, Rodríguez-
713 Tudela JL, Casadevall A. 2010. Fungal Cell Gigantism during Mammalian Infection.
714 PLoS Pathog 6:e1000945.

715 46. Gerstein AC, Fu MS, Mukaremera L, Li Z, Ormerod KL, Fraser JA, Berman J,
716 Nielsen K. 2015. Polyploid Titan Cells Produce Haploid and Aneuploid Progeny To
717 Promote Stress Adaptation. MBio 6:e01340-15.

718 47. Hommel B, Mukaremera L, Cordero RJB, Coelho C, Desjardins CA, Sturny-Leclère
719 A, Janbon G, Perfect JR, Fraser JA, Casadevall A, Cuomo CA, Dromer F, Nielsen
720 K, Alanio A. 2018. Titan cells formation in *Cryptococcus neoformans* is finely tuned

721 by environmental conditions and modulated by positive and negative genetic
722 regulators. PLOS Pathog 14:e1006982.

723 48. Trevijano-Contador N, de Oliveira HC, García-Rodas R, Rossi SA, Llorente I,
724 Zaballos Á, Janbon G, Ariño J, Zaragoza Ó. 2018. *Cryptococcus neoformans* can
725 form titan-like cells *in vitro* in response to multiple signals. PLOS Pathog
726 14:e1007007.

727 49. Dambuza IM, Drake T, Chapuis A, Zhou X, Correia J, Taylor-Smith L, LeGrave N,
728 Rasmussen T, Fisher MC, Bicanic T, Harrison TS, Jaspars M, May RC, Brown GD,
729 Yuecel R, MacCallum DM, Ballou ER. 2018. The *Cryptococcus neoformans* Titan
730 cell is an inducible and regulated morphotype underlying pathogenesis. PLOS
731 Pathog 14:e1006978.

732 50. García-Barbazán I, Trevijano-Contador N, Rueda C, de Andrés B, Pérez-Tavárez
733 R, Herrero-Fernández I, Gaspar ML, Zaragoza O. 2016. The formation of titan cells
734 in *Cryptococcus neoformans* depends on the mouse strain and correlates with
735 induction of Th2-type responses. Cell Microbiol 18:111–124.

736 51. Mukaremera L, Lee KK, Wagener J, Wiesner DL, Gow NAR, Nielsen K. 2018. Titan
737 cell production in *Cryptococcus neoformans* reshapes the cell wall and capsule
738 composition during infection. Cell Surf 1:15–24.

739 52. Jung K-W, Yang D-H, Maeng S, Lee K-T, So Y-S, Hong J, Choi J, Byun H-J, Kim
740 H, Bang S, Song M-H, Lee J-W, Kim MS, Kim S-Y, Ji J-H, Park G, Kwon H, Cha S,
741 Meyers GL, Wang LL, Jang J, Janbon G, Adedoyin G, Kim T, Averette AK,
742 Heitman J, Cheong E, Lee Y-H, Lee Y-W, Bahn Y-S. 2015. Systematic functional
743 profiling of transcription factor networks in *Cryptococcus neoformans*. Nat Commun

744 6:6757.

745 53. Schneider R de O, Fogaça N de SS, Kmetzsch L, Schrank A, Vainstein MH, Staats
746 CC. 2012. Zap1 Regulates Zinc Homeostasis and Modulates Virulence in
747 *Cryptococcus gattii*. PLoS One 7:e43773.

748 54. Garcia-Santamarina S, Festa RA, Smith AD, Yu C-H, Probst C, Ding C, Homer
749 CM, Yin J, Noonan JP, Madhani H, Perfect JR, Thiele DJ. 2018. Genome-wide
750 analysis of the regulation of Cu metabolism in *Cryptococcus neoformans*. Mol
751 Microbiol 108:473–494.

752 55. Lev S, Kaufman-Francis K, Desmarini D, Juillard PG, Li C, Stifter SA, Feng CG,
753 Sorrell TC, Grau GER, Bahn Y-S, Djordjevic JT. 2017. Pho4 Is Essential for
754 Dissemination of *Cryptococcus neoformans* to the Host Brain by Promoting
755 Phosphate Uptake and Growth at Alkaline pH. mSphere 2:e00381-16.

756 56. Jung WH, Sham A, White R, Kronstad JW. 2006. Iron Regulation of the Major
757 Virulence Factors in the AIDS-Associated Pathogen *Cryptococcus neoformans*.
758 PLoS Biol 4:e410.

759 57. Chow EWL, Clancey SA, Billmyre RB, Averette AF, Granek JA, Mieczkowski P,
760 Cardenas ME, Heitman J. 2017. Elucidation of the calcineurin-Crz1 stress
761 response transcriptional network in the human fungal pathogen *Cryptococcus*
762 *neoformans*. PLOS Genet 13:e1006667.

763 58. O'Meara TR, Norton D, Price MS, Hay C, Clements MF, Nichols CB, Alspaugh JA.
764 2010. Interaction of *Cryptococcus neoformans* Rim101 and Protein Kinase A
765 Regulates Capsule. PLoS Pathog 6:e1000776.

766 59. Gish SR, Maier EJ, Haynes BC, Santiago-Tirado FH, Srikanta DL, Ma CZ, Li LX,
767 Williams M, Crouch EC, Khader SA, Brent MR, Doering TL. 2016. Computational
768 Analysis Reveals a Key Regulator of Cryptococcal Virulence and Determinant of
769 Host Response. MBio 7:e00313-16.

770 60. Chun CD, Brown JCS, Madhani HD. 2011. A Major Role for Capsule-Independent
771 Phagocytosis-Inhibitory Mechanisms in Mammalian Infection by *Cryptococcus*
772 *neoformans*. Cell Host Microbe 9:243–251.

773 61. Moranova Z, Virtudazo E, Hricova K, Ohkusu M, Kawamoto S, Husickova V,
774 Raclavsky V. 2014. The CRZ1/SP1-like gene links survival under limited aeration,
775 cell integrity and biofilm formation in the pathogenic yeast *Cryptococcus*
776 *neoformans*. Biomed Pap 158:212–220.

777 62. Lev S, Desmarini D, Chayakulkeeree M, Sorrell TC, Djordjevic JT. 2012. The
778 Crz1/Sp1 Transcription Factor of *Cryptococcus neoformans* Is Activated by
779 Calcineurin and Regulates Cell Wall Integrity. PLoS One 7:e51403.

780 63. Park H-S, Chow EWL, Fu C, Soderblom EJ, Moseley MA, Heitman J, Cardenas
781 ME. 2016. Calcineurin Targets Involved in Stress Survival and Fungal Virulence.
782 PLOS Pathog 12:e1005873.

783 64. Lee D, Jang E-H, Lee M, Kim S-W, Lee Y, Lee K-T, Bahn Y-S. 2019. Unraveling
784 Melanin Biosynthesis and Signaling Networks in *Cryptococcus neoformans*. MBio
785 10:e02267-19.

786 65. Rhodes J, Desjardins CA, Sykes SM, Beale MA, Vanhove M, Sakthikumar S, Chen
787 Y, Gujja S, Saif S, Chowdhary A, Lawson DJ, Ponzio V, Colombo AL, Meyer W,

788 Engelthaler DM, Hagen F, Illnait-Zaragozi MT, Alanio A, Vreulink J-M, Heitman J,
789 Perfect JR, Litvintseva AP, Bicanic T, Harrison TS, Fisher MC, Cuomo CA. 2017.
790 Tracing Genetic Exchange and Biogeography of *Cryptococcus neoformans* var.
791 *grubii* at the Global Population Level. Genetics 207:327–346.

792 66. Liu OW, Chun CD, Chow ED, Chen C, Madhani HD, Noble SM. 2008. Systematic
793 Genetic Analysis of Virulence in the Human Fungal Pathogen *Cryptococcus*
794 *neoformans*. Cell 135:174–188.

795 67. Lee K-T, Hong J, Lee D-G, Lee M, Cha S, Lim Y-G, Jung K-W, Hwangbo A, Lee Y,
796 Yu S-J, Chen Y-L, Lee J-S, Cheong E, Bahn Y-S. 2020. Fungal kinases and
797 transcription factors regulating brain infection in *Cryptococcus neoformans*. Nat
798 Commun 11:1521.

799 68. Krysan DJ, Zhai B, Beattie SR, Misel KM, Wellington M, Lin X. 2019. Host Carbon
800 Dioxide Concentration Is an Independent Stress for *Cryptococcus neoformans* That
801 Affects Virulence and Antifungal Susceptibility. MBio 10:e01410-19.

802 69. D'Souza CA, Alspaugh JA, Yue C, Harashima T, Cox GM, Perfect JR, Heitman J.
803 2001. Cyclic AMP-Dependent Protein Kinase Controls Virulence of the Fungal
804 Pathogen *Cryptococcus neoformans*. Mol Cell Biol 21:3179–3191.

805 70. Hu G, Steen BR, Lian T, Sham AP, Tam N, Tangen KL, Kronstad JW. 2007.
806 Transcriptional Regulation by Protein Kinase A in *Cryptococcus neoformans*. PLoS
807 Pathog 3:e42.

808 71. Yoneda A, Doering TL. 2008. Regulation of *Cryptococcus neoformans* Capsule
809 Size Is Mediated at the Polymer Level. Eukaryot Cell 7:546–549.

810 72. Frases S, Pontes B, Nimrichter L, Viana NB, Rodrigues ML, Casadevall A. 2009.
811 Capsule of *Cryptococcus neoformans* grows by enlargement of polysaccharide
812 molecules. Proc Natl Acad Sci U S A 106:1228–1233.

813 73. Gaylord EA, Choy HL, Doering TL. 2020. Dangerous Liaisons: Interactions of
814 *Cryptococcus neoformans* with Host Phagocytes. Pathogens 9:891.

815 74. Bailey TL. 2011. DREME: Supp. Bioinformatics 27:1653–1659.

816 75. Summers DK, Perry DS, Rao B, Madhani HD. 2020. Coordinate genomic
817 association of transcription factors controlled by an imported quorum sensing
818 peptide in *Cryptococcus neoformans*. PLOS Genet 16:e1008744.

819 76. Homer CM, Summers DK, Goranov AI, Clarke SC, Wiesner DL, Diedrich JK,
820 Moresco JJ, Toffaletti D, Upadhya R, Caradonna I, Petnic S, Pessino V, Cuomo
821 CA, Lodge JK, Perfect J, Yates 3rd JR, Nielsen K, Craik CS, Madhani HD. 2016.
822 Intracellular Action of a Secreted Peptide Required for Fungal Virulence. Cell Host
823 Microbe 19:849–864.

824 77. Kang Y, Patel NR, Shively C, Recio PS, Chen X, Wranik BJ, Kim G, Scott McIsaac
825 R, Mitra R, Brent MR. 2020. Dual threshold optimization and network inference
826 reveal convergent evidence from TF binding locations and TF perturbation
827 responses. Genome Res 30:459–471.

828 78. Giles SS, Stajich JE, Nichols C, Gerrald QD, Alspaugh JA, Dietrich F, Perfect JR.
829 2006. The *Cryptococcus neoformans* catalase gene family and its role in
830 antioxidant defense. Eukaryot Cell 5:1447–1459.

831 79. Cox GM, Harrison TS, McDade HC, Taborda CP, Heinrich G, Casadevall A,

832 Perfect JR. 2003. Superoxide dismutase influences the virulence of *Cryptococcus*
833 *neoformans* by affecting growth within macrophages. Infect Immun 71:173–80.

834 80. Lee K-T, So Y-S, Yang D-H, Jung K-W, Choi J, Lee D-G, Kwon H, Jang J, Wang
835 LL, Cha S, Meyers GL, Jeong E, Jin J-H, Lee Y, Hong J, Bang S, Ji J-H, Park G,
836 Byun H-J, Park SW, Park Y-M, Adedoyin G, Kim T, Averette AF, Choi J-S, Heitman
837 J, Cheong E, Lee Y-H, Bahn Y-S. 2016. Systematic functional analysis of kinases
838 in the fungal pathogen *Cryptococcus neoformans*. Nat Commun 7:12766.

839 81. Caza M, Hu G, Price M, Perfect JR, Kronstad JW. 2016. The Zinc Finger Protein
840 Mig1 Regulates Mitochondrial Function and Azole Drug Susceptibility in the
841 Pathogenic Fungus *Cryptococcus neoformans*. mSphere 1.

842 82. Chen Y, Toffaletti DL, Tenor JL, Litvintseva AP, Fang C, Mitchell TG, McDonald
843 TR, Nielsen K, Boulware DR, Bicanic T, Perfect JR. 2014. The *Cryptococcus*
844 *neoformans* transcriptome at the site of human meningitis. MBio 5:e01087-13.

845 83. Alspaugh JA, Pukkila-Worley R, Harashima T, Cavallo LM, Funnell D, Cox GM,
846 Perfect JR, Kronstad JW, Heitman J. 2002. Adenylyl cyclase functions downstream
847 of the Gα protein Gpa1 and controls mating and pathogenicity of *Cryptococcus*
848 *neoformans*. Eukaryot Cell 1:75–84.

849 84. Heung LJ, Kaiser AE, Luberto C, Del Poeta M. 2005. The role and mechanism of
850 diacylglycerol-protein kinase C1 signaling in melanogenesis by *Cryptococcus*
851 *neoformans*. J Biol Chem 280:28547–28555.

852 85. Gerik KJ, Bhimireddy SR, Ryerse JS, Specht CA, Lodge JK. 2008. PKC1 is
853 essential for protection against both oxidative and nitrosative stresses, cell integrity,

854 and normal manifestation of virulence factors in the pathogenic fungus
855 *Cryptococcus neoformans*. Eukaryot Cell 7:1685–1698.

856 86. Waterman SR, Hacham M, Hu G, Zhu X, Park Y-D, Shin S, Panepinto J, Valyi-
857 Nagy T, Beam C, Husain S, Singh N, Williamson PR. 2007. Role of a CUF1/CTR4
858 copper regulatory axis in the virulence of *Cryptococcus neoformans*. J Clin Invest
859 117:794–802.

860 87. Jiang N, Sun N, Xiao D, Pan J, Wang Y, Zhu X. 2009. A copper-responsive factor
861 gene *CUF1* required for copper induction of laccase in *Cryptococcus neoformans*.
862 FEMS Microbiol Lett 296:84–90.

863 88. Walton FJ, Idnurm A, Heitman J. 2005. Novel gene functions required for
864 melanization of the human pathogen *Cryptococcus neoformans*. Mol Microbiol
865 57:1381–1396.

866 89. Cheon SA, Jung K-W, Chen Y-L, Heitman J, Bahn Y-S, Kang HA. 2011. Unique
867 Evolution of the UPR Pathway with a Novel bZIP Transcription Factor, Hxl1, for
868 Controlling Pathogenicity of *Cryptococcus neoformans*. PLoS Pathog 7:e1002177.

869 90. Hicks JK, Bahn YS, Heitman J. 2005. Pde1 phosphodiesterase modulates cyclic
870 AMP levels through a protein kinase A-mediated negative feedback loop in
871 *Cryptococcus neoformans*. Eukaryot Cell 4:1971–1981.

872 91. Kozubowski L, Lee SC, Heitman J. 2009. Signalling pathways in the pathogenesis
873 of *Cryptococcus*. Cell Microbiol 11:370–380.

874 92. Fox DS, Cruz MC, Sia RAL, Ke H, Cox GM, Cardenas ME, Heitman J. 2001.
875 Calcineurin regulatory subunit is essential for virulence and mediates interactions

876 with FKBP12-FK506 in *Cryptococcus neoformans*. Mol Microbiol 39:835–849.

877 93. Odom A. 1997. Calcineurin is required for virulence of *Cryptococcus neoformans*.
878 EMBO J 16:2576–2589.

879 94. Jung W-H, Son Y-E, Oh S-H, Fu C, Kim HS, Kwak J-H, Cardenas ME, Heitman J,
880 Park H-S. 2018. Had1 Is Required for Cell Wall Integrity and Fungal Virulence in
881 *Cryptococcus neoformans*. Genes|Genomes|Genetics 8:643–652.

882 95. Kmetzsch L, Staats CC, Cupertino JB, Fonseca FL, Rodrigues ML, Schrank A,
883 Vainstein MH. 2013. The calcium transporter Pmc1 provides Ca2+ tolerance and
884 influences the progression of murine cryptococcal infection. FEBS J 280:4853–
885 4864.

886 96. Kmetzsch L, Staats CC, Simon E, Fonseca FL, de Oliveira DL, Sobrino L,
887 Rodrigues J, Leal AL, Nimrichter L, Rodrigues ML, Schrank A, Vainstein MH. 2010.
888 The Vacuolar Ca2+ Exchanger Vcx1 Is Involved In Calcineurin-Dependent Ca2+
889 Tolerance and Virulence in *Cryptococcus neoformans*. Eukaryot Cell 9:1798–1805.

890 97. Denham S, Brown J. 2018. Mechanisms of Pulmonary Escape and Dissemination
891 by *Cryptococcus neoformans*. J Fungi 4:25.

892 98. Sun D, Sun P, Li H, Zhang M, Liu G, Strickland AB, Chen Y, Fu Y, Xu J, Yosri M,
893 Nan Y, Zhou H, Zhang X, Shi M. 2019. Fungal dissemination is limited by liver
894 macrophage filtration of the blood. Nat Commun 10:4566.

895 99. Santiago-Tirado FH, Doering TL. 2017. False friends: Phagocytes as Trojan horses
896 in microbial brain infections. PLOS Pathog 13:e1006680.

897 100. Squizani ED, Oliveira NK, Reuwsaat JCV, Marques BM, Lopes W, Gerber AL, de

898 Vasconcelos ATR, Lev S, Djordjevic JT, Schrank A, Vainstein MH, Staats CC,
899 Kmetzsch L. 2018. Cryptococcal dissemination to the central nervous system
900 requires the vacuolar calcium transporter Pmc1. Cell Microbiol 20:e12803.

901 101. Okagaki LH, Nielsen K. 2012. Titan Cells Confer Protection from Phagocytosis in
902 *Cryptococcus neoformans* Infections. Eukaryot Cell 11:820–826.

903 102. Srikanta D, Santiago-Tirado FH, Doering TL. 2014. *Cryptococcus neoformans*:
904 historical curiosity to modern pathogen. Yeast 31:47–60.

905 103. Nielsen K, Cox GM, Wang P, Toffaletti DL, Perfect JR, Heitman J. 2003. Sexual
906 Cycle of *Cryptococcus neoformans* var. *grubii* and Virulence of Congenic a and α
907 Isolates. Infect Immun 71:4831–4841.

908 104. Reuwsaat JCV, Motta H, Garcia AWA, Vasconcelos CB, Marques BM, Oliveira NK,
909 Rodrigues J, Ferrareze PAG, Frases S, Lopes W, Barcellos VA, Squizani ED,
910 Horta JA, Schrank A, Rodrigues ML, Staats CC, Vainstein MH, Kmetzsch L. 2018.
911 A Predicted Mannoprotein Participates in *Cryptococcus gattii* Capsular Structure.
912 mSphere 3:e00023-18.

913 105. Haynes BC, Skowyra ML, Spencer SJ, Gish SR, Williams M, Held EP, Brent MR,
914 Doering TL. 2011. Toward an Integrated Model of Capsule Regulation in
915 *Cryptococcus neoformans*. PLoS Pathog 7:e1002411.

916 106. Babraham Bioinformatics - FastQC A Quality Control tool for High Throughput
917 Sequence Data.

918 107. Friedman RZ, Gish SR, Brown H, Brier L, Howard N, Doering TL, Brent MR. 2018.
919 Unintended Side Effects of Transformation Are Very Rare in *Cryptococcus*

920 *neoformans*. Genes|Genomes|Genetics 8:815–822.

921 108. Sedlazeck FJ, Rescheneder P, von Haeseler A. 2013. NextGenMap: fast and
922 accurate read mapping in highly polymorphic genomes. Bioinformatics 29:2790–1.

923 109. Li H, Handsaker B, Wysoker A, Fennell T, Ruan J, Homer N, Marth G, Abecasis G,
924 Durbin R, 1000 Genome Project Data Processing Subgroup. 2009. The Sequence
925 Alignment/Map format and SAMtools. Bioinformatics 25:2078–2079.

926 110. Zhang Y, Liu T, Meyer CA, Eeckhoute J, Johnson DS, Bernstein BE, Nussbaum C,
927 Myers RM, Brown M, Li W, Liu XS. 2008. Model-based Analysis of ChIP-Seq
928 (MACS). Genome Biol 9:R137.

929 111. Heinz S, Benner C, Spann N, Bertolino E, Lin YC, Laslo P, Cheng JX, Murre C,
930 Singh H, Glass CK. 2010. Simple combinations of lineage-determining transcription
931 factors prime cis-regulatory elements required for macrophage and B cell identities.
932 Mol Cell 38:576–89.

933 112. Novocraft. www.novocraft.com.

934 113. Anders S, Pyl PT, Huber W. 2015. HTSeq--a Python framework to work with high-
935 throughput sequencing data. Bioinformatics 31:166–169.

936 114. Love MI, Huber W, Anders S. 2014. Moderated estimation of fold change and
937 dispersion for RNA-seq data with DESeq2. Genome Biol 15:550.

938 115. Ignatiadis N, Klaus B, Zaugg JB, Huber W. 2016. Data-driven hypothesis weighting
939 increases detection power in genome-scale multiple testing. Nat Methods 13:577–
940 580.

941 116. Li LX, Rautengarten C, Heazlewood JL, Doering TL. 2018. Xylose donor transport
942 is critical for fungal virulence. PLOS Pathog 14:e1006765.

943

944 **ACKNOWLEDGMENTS**

945 We appreciate helpful discussions with Charley Christian Staats, Augusto Schrank, and
946 members of the Doering, Kmetzsch and Brent labs. We are grateful for assistance from
947 Thomas Hurtaux, Eamim Squizani, and Julia Sperotto with mouse experiments; Guohua
948 Chen with spotting assays; Jessica Plaggenberg with library preparation and sequencing;
949 Chase Mateusiak with RNA-seq data analysis; and Sandeep Acharya for performing the
950 DTO analysis. We thank Marilene Henning Vainstein and her lab for providing support
951 with *in vivo* experiments. We also thank Liza Miller for comments on the manuscript and
952 Arturo Casadevall for providing the antibody anti-GXM (18B7).

953 These studies were supported by National Institutes of Health grant AI087794 to TLD and
954 MRB; National Institutes of Health grants AI36688 and AI140979 to TLD; and grants from
955 Coordenação de Aperfeiçoamento de Pessoal de Nível Superior (CAPES, Brazil),
956 Conselho Nacional de Desenvolvimento Científico e Tecnológico (CNPq, Brazil – Grant
957 number 310510/2018-0), and Fundação de Amparo à Pesquisa do Estado do Rio
958 Grande do Sul (FAPERGS, Brazil) to LK. CAPES fully supported JCVR during her
959 studies in Brazil; her studies in the United States were partially supported by this source
960 (Advanced Network of Computational Biology - RABICÓ - Biocomputational Grant
961 23038.010041/2013-13).

962

963 **AUTHORS CONTRIBUTION**

964 Conceived and designed experiments: J.C.V.R., D.P.A., A.L.C., M.R.B., L.K. and T.L.D.;

965 Performed experiments: J.C.V.R., D.P.A., H.M., H.B., and A.L.C;

966 Analyzed data: J.C.V.R., D.P.A., A.L.C., M.R.B., L.K. and T.L.D.;

967 Contributed reagents and materials: M.R.B., L.K. and T.L.D.;

968 Drafted the paper: J.C.V.R, L.K. and T.L.D.

969 Revised the paper: J.C.V.R., D.P.A., M.R.B., L.K. and T.L.D.

970

971 **COMPETING INTERESTS**

972 The authors declare no competing financial interests.

973

974 **TABLES**

975 **Table 1. Pdr802 targets involved in quorum sensing and Titan cell formation.**

976

977 **Table 2. Genes regulated by Pdr802 involved in adaptation to the host**

978 **environment.**

979

980 **FIGURE LEGENDS**

981 **Figure 1. The transcription factor Pdr802 influences *C. neoformans* virulence.** A.
982 Survival of C57BL/6 mice over time after intranasal inoculation with 5 x 10^4 cryptococci of
983 the strains indicated, with sacrifice triggered by weight below 80% of peak. B. Mean +/-
984 SD of total colony-forming units (CFU) in lung tissue at various times post-infection. CFU
985 inoculated for each strain were 41,400 (KN99α), 42,800 (*pdr802*) and 26,600 (*PDR802*).
986 $p<0.05$ for *pdr802* compared to the other strains at all time points.

987

988 **Figure 2. *PDR802* expression is required for cell viability and induced during**
989 **growth in host-like conditions.** A. Cells grown in DMEM at 37°C and 5% CO_2 were
990 sampled at the times indicated and plated on YPD to assess viability (measured by CFU
991 and plotted as fold-change from time 0). B. *PDR802* expression in KN99α cells grown in
992 DMEM at 37°C and 5% CO_2 was assessed by RNA-seq as in Li *et al*., 2018 (116).

993

994 **Figure 3. The *pdr802* mutant is hypercapsular.** A. Representative
995 immunofluorescence micrographs of the indicated strains after growth in DMEM (37°C,
996 5% CO_2) for 24 hours. The capsule was stained with monoclonal antibody anti-GXM 302
997 conjugated with Alexa 488 (green) and the cell wall with Calcofluor White (blue). All
998 images are to the same scale; scale bar, 5 μm. B. Capsule thickness distribution for the
999 indicated strains. C. Mean +/- SD of capsule size, quantified as detailed in the Methods
1000 and Figure S5, with *pkr1* (39) and *ada2* (105) shown as hypercapsular and hypocapsular
1001 controls, respectively. ****, $p<0.0001$ compared to KN99α by one-way ANOVA with
1002 posthoc Dunnett test.

1003

1004 **Figure 4. Growth in mouse serum elicits increased capsule thickness and cell body**
1005 **diameter in the *pdr802* mutant.** A. Light micrographs of the indicated strains after
1006 growth in mouse serum (at 37°C, 5% CO_2) for 24 h and negative staining with India ink to
1007 visualize the capsule. All images are to the same scale; scale bar, 5 μm. B. Mean +/- SD
1008 of capsule thickness, assessed by measuring at least 50 cells per strain with ImageJ. C.
1009 Cells grown as in Panel A were plated on YPD to assess CFU. Mean +/- SD of the fold-
1010 change compared to 0 h is shown. D. Mean +/- SD of cell body diameter, measured as in
1011 B. ***, $p<0.001$ and ****, $p<0.0001$ for comparison of *pdr802* results to KN99α by one-
1012 way ANOVA with posthoc Dunnett test.

1013

1014 **Figure 5. Absence of *PDR802* yields enlarged cells and loss of capsule induction in**
1015 **the context of animal infection.** A. India ink staining of fungi isolated from the lungs of
1016 mice infected with the indicated strains. Numbers at left indicate the days post-infection.
1017 All images are to the same scale; scale bar, 10 μm. B and C. Mean +/- SD of cell body
1018 diameter (B) and capsule thickness (C), assessed by measuring at least 50 cells per
1019 strain with ImageJ. ****, $p<0.0001$ and ***, $p<0.001$ for comparison of *pdr802* results to
1020 KN99α or *PDR802* by one-way ANOVA with posthoc Dunnett test for each day post-
1021 infection.

1022

1023 **Figure 6. Pdr802 is a negative regulator of Titan cell formation.** Left, cultures were
1024 subjected to *in vitro* conditions that induce Titan cell formation and imaged with India Ink.
1025 All images are to the same scale; scale bar, 10 μm. Images were selected so that each
1026 shows multiple examples of Titan cells, not to reflect abundance of this morphotype.

1027 Right, the percent of Titan cells (TC) in each culture was quantified using flow cytometry,
1028 gated as indicated by the blue square. FSC, forward scatter; SSC, side scatter.

1029

1030 **Figure 7. Deletion of *PDR802* affects phagocytosis after growth under conditions**
1031 **that induce capsule and Titan cell formation.** The indicated *C. neoformans* strains
1032 were grown in YPD (18 h), DMEM (24 h), or Titan-cell induction medium (72 h) and then
1033 incubated for 2 h with J774.16 mouse macrophages; host cells were then washed and
1034 lysed to assess fungal burden by CFU. Data shown are normalized to the CFU of the
1035 initial inoculum. *, $p<0.05$ and **, $p<0.01$ compared to KN99α by one-way ANOVA with
1036 posthoc Dunnett test.

1037

1038 **Figure 8. Pdr802 participates in calcineurin signaling.** *Panels A-B*. Interactions of
1039 Pdr802 with upstream regions of the indicated genes. The ratios ($\log_2$) of reads from
1040 immunoprecipitated (IP) DNA to input DNA were calculated for 1,000 bp upstream of the
1041 first coding nucleotide (+1); shown is the difference in these values between tagged and
1042 untagged strains. Black triangles, complete Pdr802 DNA-binding motifs (Figure S7B);
1043 gray triangles, partial motifs. C. Intracellular calcium measurement by flow cytometry
1044 using Fluo-4AM. Each column shows the mean and standard deviation of three biological
1045 replicates. ***, $p<0.001$ and ****, $p<0.0001$ by one-way ANOVA with posthoc Dunnett
1046 test.

1047

1048 **Figure 9. Pdr802 mode of action.** *Left panel*. When wild-type *C. neoformans* enters a
1049 host, *PDR802* expression is induced and Pdr802 positively regulates elements of the
1050 quorum sensing pathway (described in the text) as well as expression of TFs implicated
1051 in this pathway (*LIV3*), brain infectivity (*STB4*), and Titan cell production (*ZFC3*). At the
1052 same time, Pdr802 regulates two calcineurin targets (*CRZ1* and *HAD1*) and a variety of
1053 other genes (see text). Shown are examples of genes involved in the response to
1054 oxidative stress (*SOD1*), growth at 37°C (*KIC1*), urease activity (*GUT1*), capsule
1055 production (*BZP4*), and cell wall remodeling (*MP98*). *Right panel*. In the absence of these
1056 regulatory changes, *pdr802* cells are poorly equipped to survive the stress of the host
1057 environment and are subject to increased intracellular calcium levels, dysregulation of
1058 capsule production, and impaired stress resistance. As a result, the cryptococcal
1059 population in the lung is smaller and is enriched in Titan cells and hypercapsular cells of
1060 normal size, both of which demonstrate reduced phagocytosis by host cells and impaired
1061 ability to cross biological barriers; these defects reduce dissemination to the central
1062 nervous system.

1063

1064 **SUPPLEMENTAL FIGURE LEGENDS**

1065 **Figure S1. Mutant strain construction and confirmation.** A. Scheme for generating *C.*
1066 *neoformans* strains in the KN99α background (middle) that either lack *PDR802* (*pdr802,*
1067 top) or encode a tagged copy of the protein (*mCherry-PDR802*). B. Qualitative analysis of
1068 gene expression in Panel A strains and the complemented *pdr802* mutant (*PDR802*).
1069 Cryptococcal mRNA isolated from cells grown in DMEM (37°C, 5% CO_2, 24 hours) was
1070 used to generate cDNA; from this, segments of the genes indicated at the left were

1071 amplified using the primers listed in Data Set S2, Sheet 5, and the products were
1072 analyzed by agarose gel electrophoresis. Fragment sizes (in bp) are indicated at right
1073 and the ladder bands shown are 400, 500, 650, 850 and 1000 bp for the top panel; 200,
1074 300, 400, 500, and 650 bp for the middle panel; and 100, 200, and 300 bp for the bottom
1075 panel. C. Quantitative analysis of *PDR802* expression. Samples of RNA isolated as in B
1076 were analyzed for *PDR802* expression by qRT-PCR. All results were normalized to *ACT1*
1077 expression. Each symbol represents a biological replicate, with the mean and standard
1078 deviation also shown. ***, $p<0.001$ compared to KN99α by one-way ANOVA with posthoc
1079 Dunnett test.

1080

1081 **Figure S2. Organ burdens.** A. Mean +/- SD values of total colony-forming units (CFU) in
1082 the indicated tissue of mice from the Figure 1 survival curve are shown. Each point is the
1083 average value for a single animal at the time of death. For *pdr802* infections, red circles
1084 represent mice sacrificed at days 65 and 69, while blue circles represent mice sacrificed
1085 at the end of the study (day 100). B. Mean +/- SD of total colony-forming units (CFU) in
1086 the blood and brain at the indicated times post-infection. C. Mean +/- SD of total colony-
1087 forming units (CFU) in the lung, blood and brain 75 days after infection with *pdr802*. Each
1088 color represents one mouse.

1089

1090 **Figure S3. Characterization of *pdr802* cells.** *Panels A-C.*10-fold serial dilutions of WT,
1091 *pdr802*, and *PDR802* cells were plated on the media shown and incubated at 30°C (A),
1092 37°C (B), or 37°C in the presence of 5% CO_2 (C). Nitrosative ($NaNO_2$) and oxidative
1093 (H_2O_2) stress plates were prepared with YNB medium and melanization plates containing

1094 L-DOPA were prepared as in the Methods; all other plates were prepared with YPD
1095 medium. *lac1*, a control strain lacking the ability to melanize (88). D. Urease activity of the
1096 indicated strains was evaluated using Christensen's urea solid medium (see Methods) at
1097 the indicated temperatures. *ure1*, a control strain that does not produce urease (17).

1098

1099 **Figure S4. Growth curves and capsule shedding.** *Panels A-B*. Growth of the strains
1100 indicated in YPD at 30°C (A) or DMEM at 37°C and 5% CO_2 (B) was assessed by
1101 OD_{600nm} at the times shown. C. Conditioned medium from the indicated strains was
1102 probed for the presence of GXM after growth in DMEM for 24 or 48 hours. Equal volumes
1103 of culture supernatant were analyzed without normalization to cell density.
1104 Immunoblotting was performed using the anti-GXM monoclonal antibody 302.

1105

1106 **Figure S5. Semi-automated assay for cryptococcal capsule imaging.** A. Schematic
1107 of applying this method to cryptococcal cells induced to form capsule by growth in DMEM
1108 (37°C, 5% CO_2) for 24 h, followed by cell wall and capsule staining. Thousands of cells
1109 may be imaged per well and analyzed automatically with software that annotates and
1110 measures the capsule (annotated on the micrograph in blue) and cell wall (annotated in
1111 bright green). See Methods for details. B. Capsule size distribution of WT cells after
1112 induction. Capsule thickness for each cell is the difference between the paired diameters
1113 of the cell wall and capsule, which is plotted here with reference to the mean value. C
1114 and D. Mean and SD (C) and cumulative percentage (D) analysis of WT compared to
1115 hyper and hypocapsular control strains (here *pkr1* and *ada2*, respectively). Capsule
1116 thickness is in arbitrary units, related to the pixels measured. E. The time required to

1117 analyze the capsule thickness of 1,000 cells by this method compared to manual
1118 assessment of India ink images.

1119

1120 **Figure S6. *PDR802* deletion induces Titan cell formation.** Mean +/- SD of (A) total cell
1121 diameter and (B) the ratio of total cell to cell body diameters (diameter ratio), assessed by
1122 measuring at least 50 cells per strain with ImageJ. **, $p<0.01$ and ****, $p<0.0001$ for
1123 comparison of *pdr802* to KN99α or *PDR802* by one-way ANOVA with posthoc Dunnett
1124 test for each day post-infection. C. Percent of Titan cells in the indicated strain, evaluated
1125 using various published parameters: cell body diameter above 10 or 15 μm (20) or total
1126 cell diameter above 30 μm (43).

1127

1128 **Figure S7. Pdr802 strain viability, putative DNA-binding motifs, and self-regulation.**
1129 A. The indicated strains were grown in DMEM at 37°C and 5% CO_2 for the times shown
1130 and samples were tested for their ability to form colonies on YPD medium. Plotted is the
1131 fold-change in CFU relative to the initial culture. B. Putative Pdr802-binding motifs
1132 determined using DREME (74). Primary and secondary hits are shown for analysis of
1133 1,000 bp upstream of the initiating ATG. C. Pdr802 self-regulation. The ratios (log_2) of
1134 reads from immunoprecipitated (IP) DNA to reads from input DNA were calculated for
1135 1,000 bp upstream of the first coding nucleotide (+1) of *PDR802*; shown is the difference
1136 in these values between tagged and untagged strains. Red triangles, complete Pdr802
1137 DNA-binding motifs (Figure S7B); blue triangles, partial motifs.

1138

1139 **Data Set S1. Pdr802 ChIP-Seq, RNA-Seq, and Dual-Threshold Optimization (DTO)**
1140 **data.** Sheet 1, peaks that occur in gene promoter regions that showed ≥2-fold enrichment
1141 when Chip-Seq was performed on strains expressing tagged versus untagged Pdr802,
1142 with annotation. Sheet 2, ChIP-Seq primary data of Pdr802-specific peaks. Sheet 3,
1143 RNA-Seq data. Sheet 4, DTO filtered data. Sheet 5, DTO primary data. Sheet 6, ChIP-
1144 Seq data of all peaks in mCherry-Pdr802 samples. Sheet 7, ChIP-Seq data of all peaks in
1145 untagged (WT) control samples.

1146

1147 **Data Set S2. Pdr802 target analysis and primers used in this study.** Sheet 1, Pdr802
1148 regulated genes that are down-regulated during Titan cell formation *in vitro* (48). Sheet 2,
1149 Pdr802 regulated genes that are up-regulated during Titan cell formation *in vitro* (48).
1150 Sheet 3, targets regulated by Pdr802 that are also dephosphorylated by calcineurin (63).
1151 Sheet 4, the intersection of Pdr802 targets and genes that are Crz1-independent
1152 calcineurin targets under conditions thermal stress (55). Sheet 6, primers used in this
1153 study. Fold enrichment and adjusted p (q) values throughout are for the DTO results.

1154

1155 **Supplementary Methods.**

Table 1. Pdr802 targets involved in quorum sensing and Titan cell formation.

Biological process	CNAG	Gene name	ChIP-seq[1]	RNA-seq[2]	Description
Quorum sensing	00150	*PQP1*	1.38	-0.78	Peptidase
	03013	*OPT1*	1.25	-0.55	OPT small oligopeptide transporter
Titan cell formation	05835	*LIV3*	1.52	-0.84	Transcription factor
	05785	*STB4*	3.33	-1.71	Transcription factor
	05940	*ZFC3/CQS2*	2.23	0.68	Transcription factor

[1]Fold-change for mCherry-Pdr802 compared to WT
[2]Log_2 fold-change for *pdr802* compared to WT

Table 2. Genes regulated by Pdr802 involved in adaptation to the host environment.

Biological process	CNAG	Gene name	ChIP-seq[1]	RNA-seq[2]	Description
Oxidative stress resistance	04981	*CAT1*	1.47	-1.60	Catalase 1
	05256	*CAT2*	1.41	-0.42	Catalase 2
	01019	*SOD1*	2.59	-0.53	Superoxide dismutase [Cu-Zn]
	00896	*FZC34*	2.22	-0.82	Transcription factor
	06327	*MIG1*	1.72	-0.78	DNA-binding protein creA
	00556	*CCK1*	1.78	-0.48	Casein kinase I
Melanin and cell wall formation	03202	*CAC1*	1.60	-0.61	Adenylate cyclase
	01845	*PKC1*	2.00	-0.48	AGC/PKC protein kinase
	07724	*CUF1*	1.27	-0.67	Metal-binding regulatory protein
	00740	*SNF5*	1.28	-0.70	Swi/snf chromatin-remodeling subunit
	01239	*CDA3*	2.63	1.08	Chitin deacetylase 3
	01230	*MP98*	2.74	0.96	Chitin deacetylase 2
	00776	*MP88*	1.86	1.23	Immunoreactive mannoprotein
Growth at 37°C	00405	*KIC1*	1.88	-0.97	Ste/ste20/ysk protein kinase
	03670	*IRE1*	1.66	-1.14	IRE protein kinase
Urease activity	07448	*DUR3*	2.13	-3.05	Urea transporter
	01209	*FAB1*	2.29	-0.49	1-phosphatidylinositol-3-P 5-kinase
	01938	*KIN1*	1.61	-0.34	CAMK/CAMKL/KIN1 protein kinase
	01155	*GUT1*	2.96	0.62	Glycerol kinase
	00791	*HLH1*	1.71	-1.09	Transcription factor
Capsule thickness	02802	*ARG2*	1.56	-0.59	Inositol/phosphatidylinositol kinase
	06809	*IKS1*	2.28	-0.44	IKS protein kinase
	01905	*KSP1*	2.02	-0.64	Serine/threonine protein kinase
	02877	*FZC51*	1.75	-0.69	Transcription factor
	07470	*PDE2*	2.42	-1.80	High-affinity phosphodiesterase
	03346	*BZP4*	3.52	1.30	Transcription factor
Calcineurin signaling	00156	*CRZ1*	1.44	-0.49	Transcription factor
	01744	*HAD1*	2.26	0.47	Phosphatase

[1]Fold-change for mCherry-Pdr802 compared to WT
[2]Log_2 fold-change for *pdr802* compared to WT

FIGURE 1

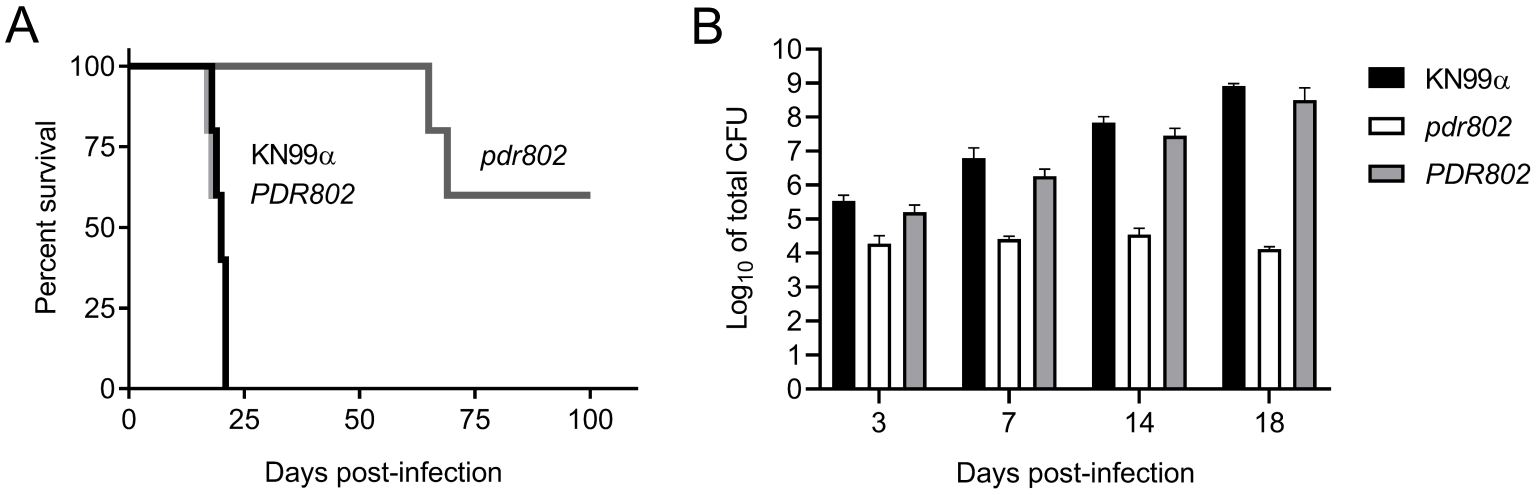
A
Percent survival
100
75
50
25
0
0
25
50
75
100
Days post-infection
KN99α
PDR802
pdr802
B
Log10 of total CFU
10
9
8
7
6
5
4
3
2
1
0
3
7
14
18
Days post-infection
KN99α
pdr802
PDR802

FIGURE 2

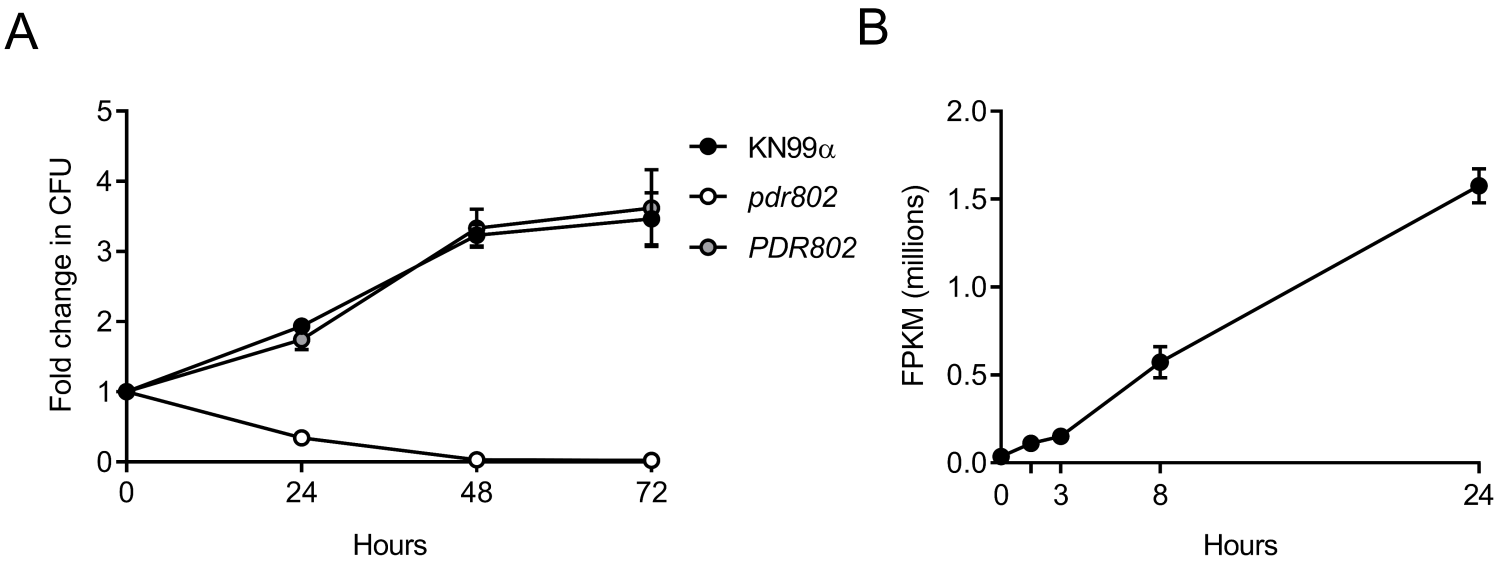
A
Fold change in CFU
5
4
3
2
1
0
0
24
48
72
Hours
KN99α
pdr802
PDR802
B
FPKM (millions)
2.0
1.5
1.0
0.5
0.0
0
3
8
24
Hours

FIGURE 3

A

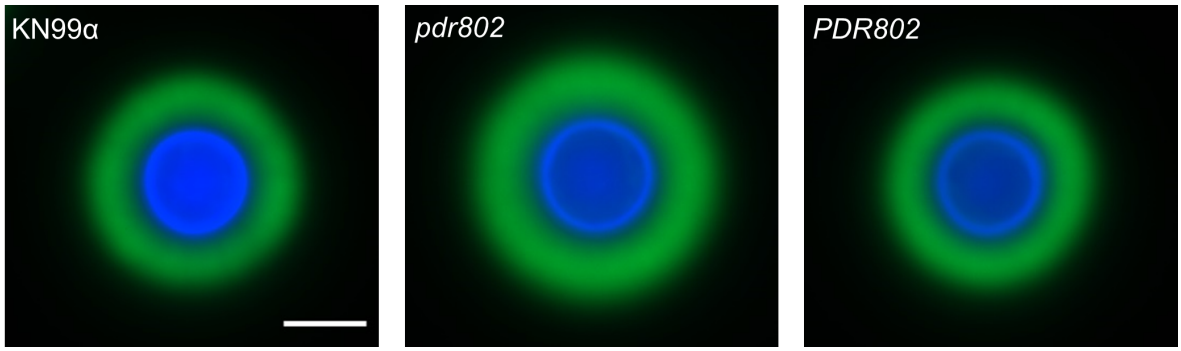
KN99α
pdr802
PDR802

B

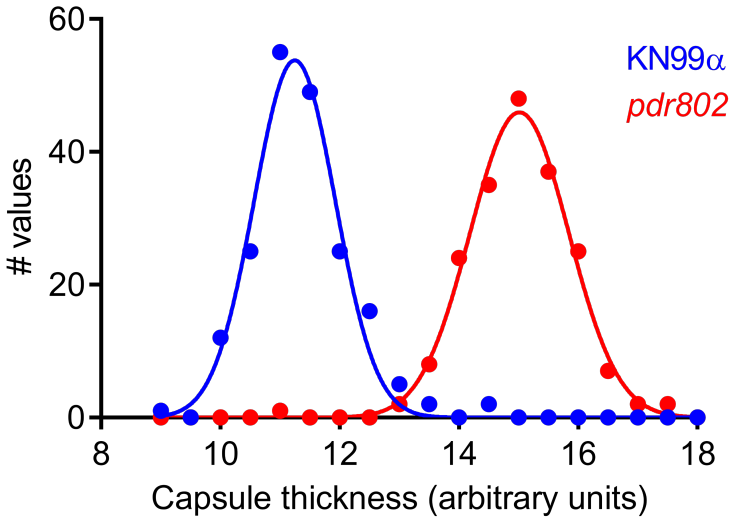
60
40
20
0
values
8
10
12
14
16
18
Capsule thickness (arbitrary units)
KN99α
pdr802

C

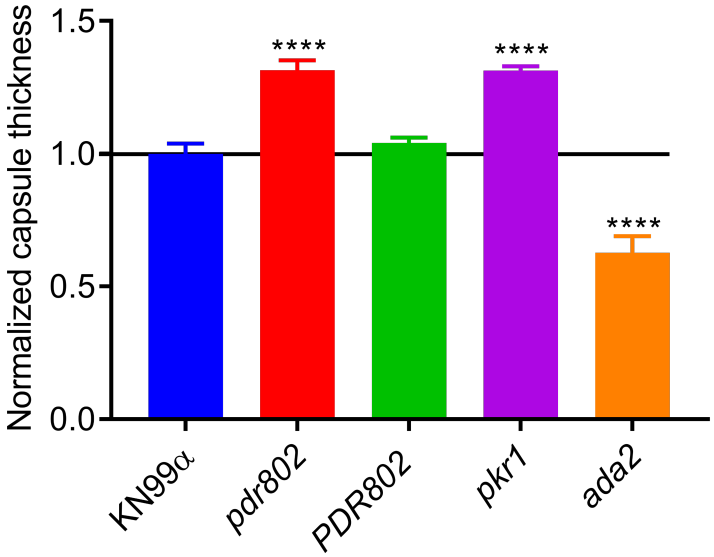
1.5
1.0
0.5
0.0
Normalized capsule thickness
****
****
****
KN99α
pdr802
PDR802
pkr1
ada2

FIGURE 4

A

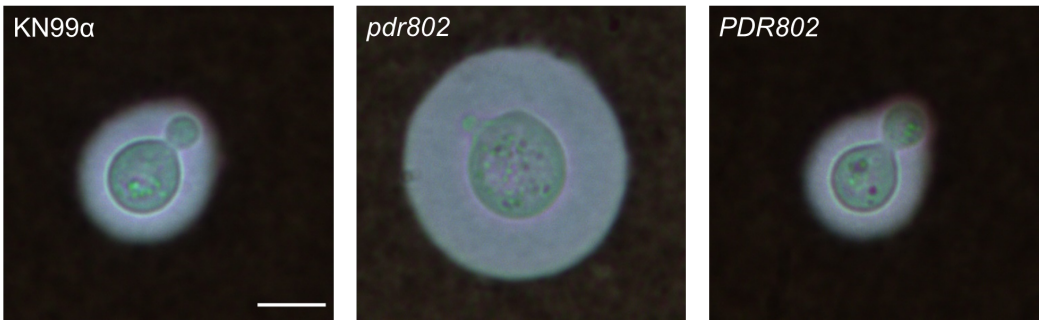

B

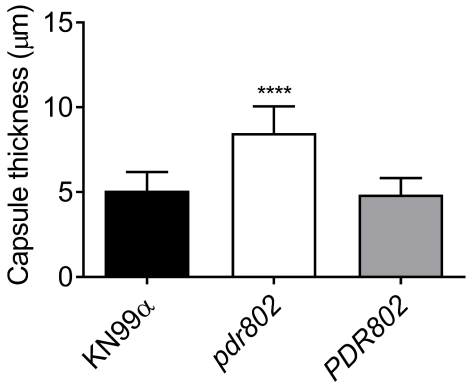

C

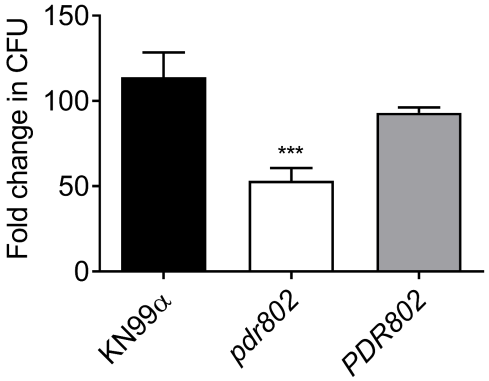

D

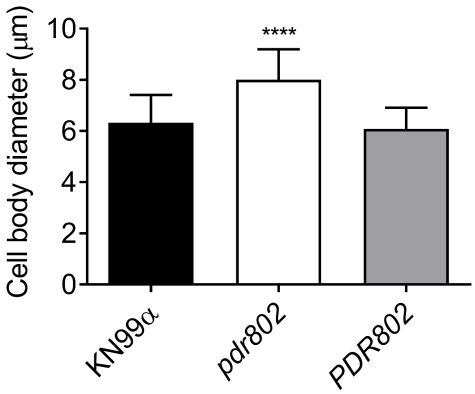

FIGURE 5

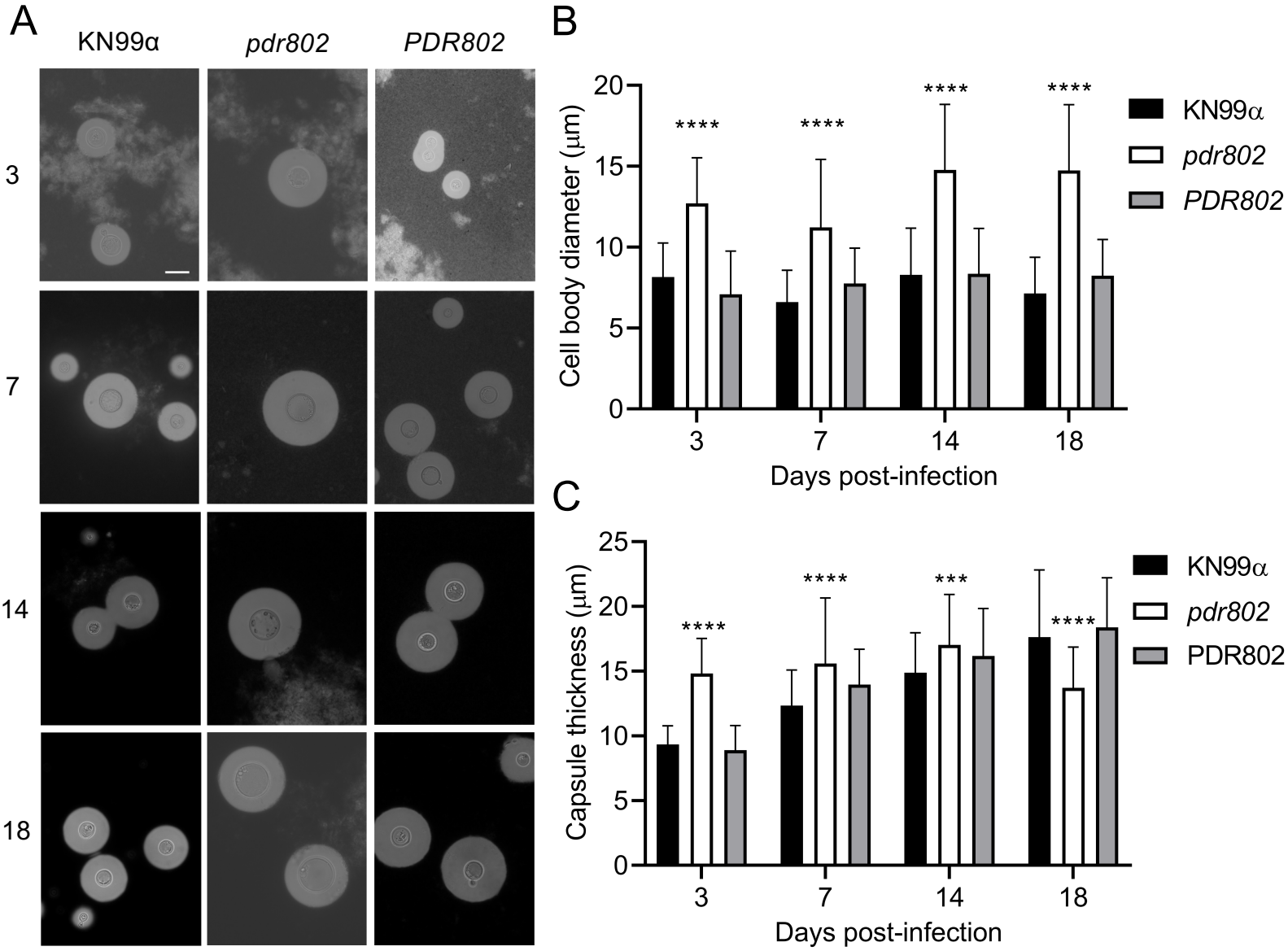
A
KN99α
pdr802
PDR802
3
7
14
18
B
Cell body diameter (μm)
20
15
10
5
0
****
****
****
****
3
7
14
18
Days post-infection
KN99α
pdr802
PDR802
C
Capsule thickness (μm)
25
20
15
10
5
0
****
****
***
****
3
7
14
18
Days post-infection
KN99α
pdr802
PDR802

FIGURE 6

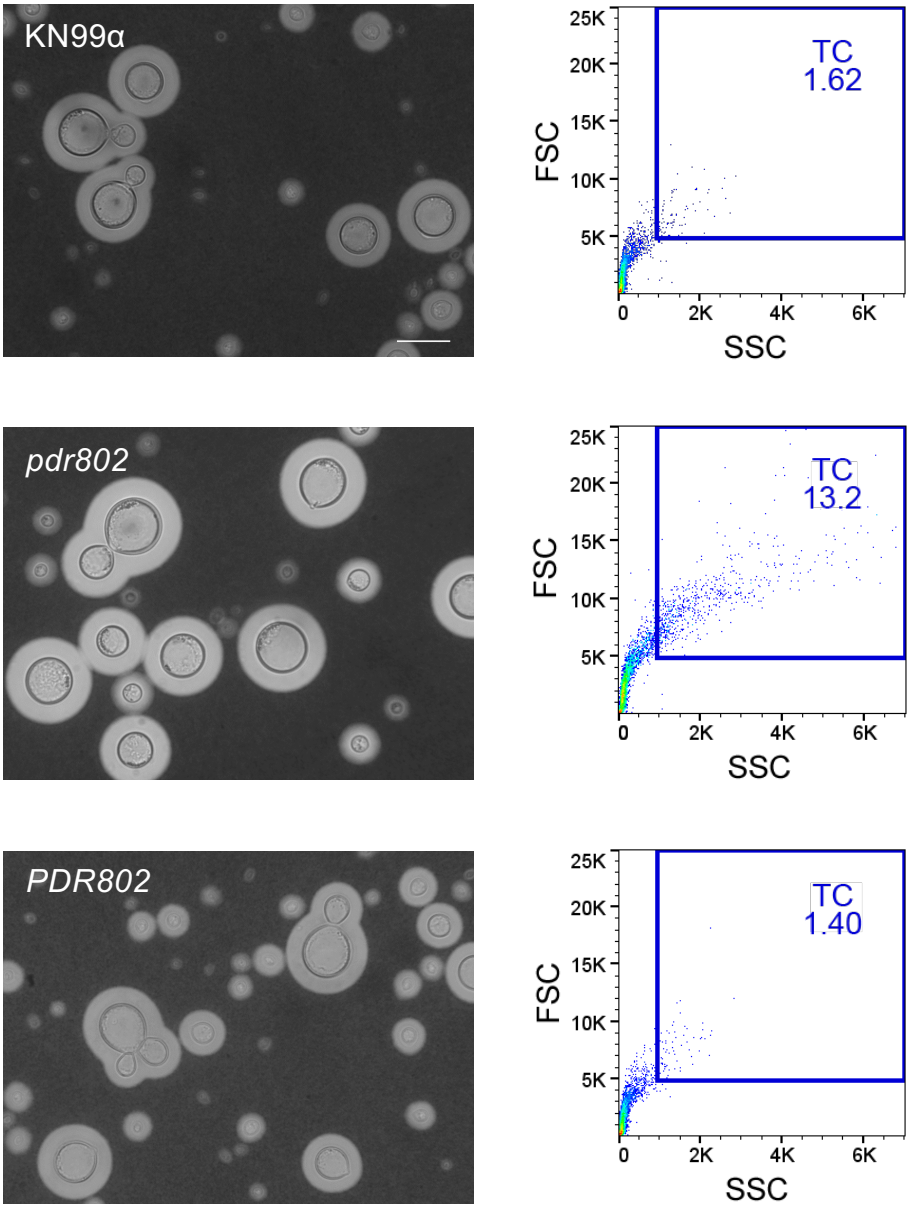
KN99α
TC
1.62
pdr802
TC
13.2
PDR802
TC
1.40
FSC
SSC
25K
20K
15K
10K
5K
0
2K
4K
6K

FIGURE 7

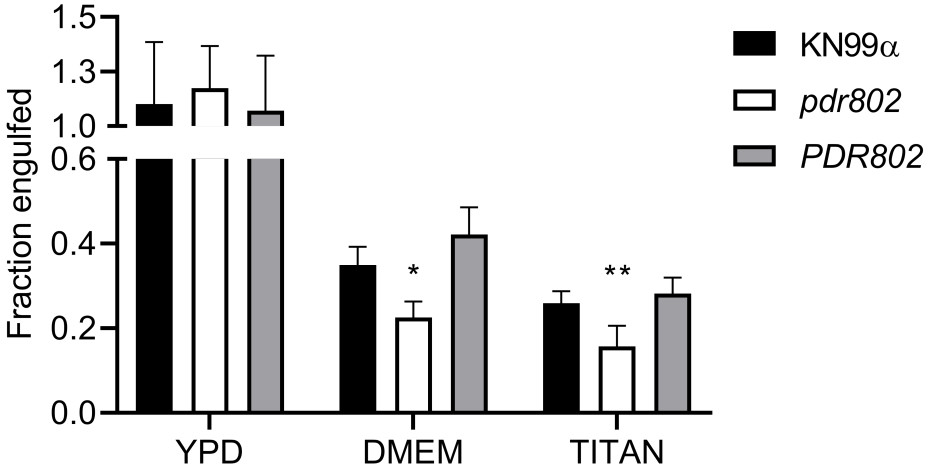
1.5
1.3
1.0
0.6
0.4
0.2
0.0
Fraction engulfed
*
**
YPD
DMEM
TITAN
KN99α
pdr802
PDR802

FIGURE 8

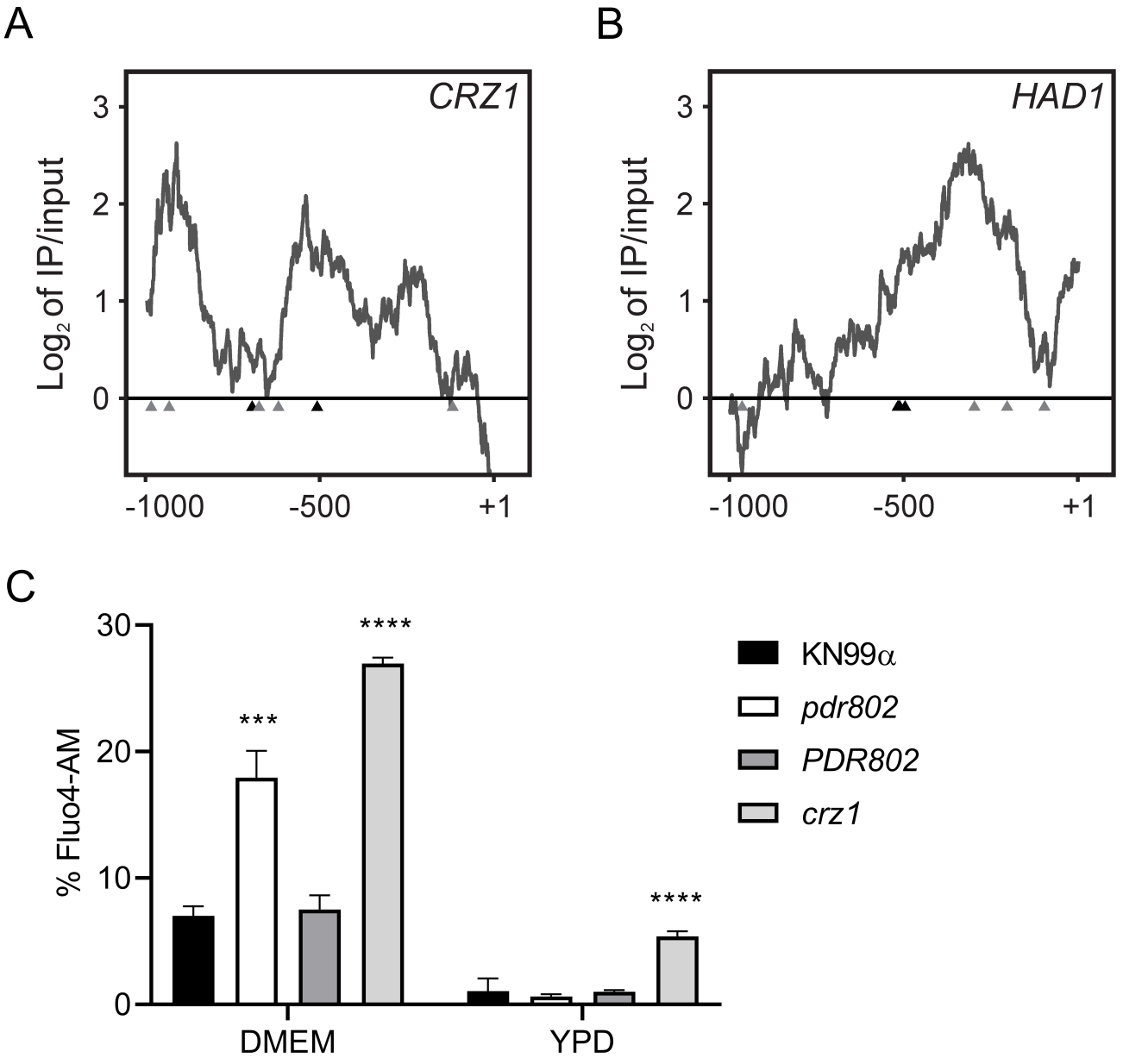
A
CRZ1
Log2 of IP/input
3
2
1
0
-1000
-500
+1
B
HAD1
Log2 of IP/input
3
2
1
0
-1000
-500
+1
C
% Fluo4-AM
30
20
10
0
***
****
****
DMEM
YPD
KN99α
pdr802
PDR802
crz1

FIGURE 9

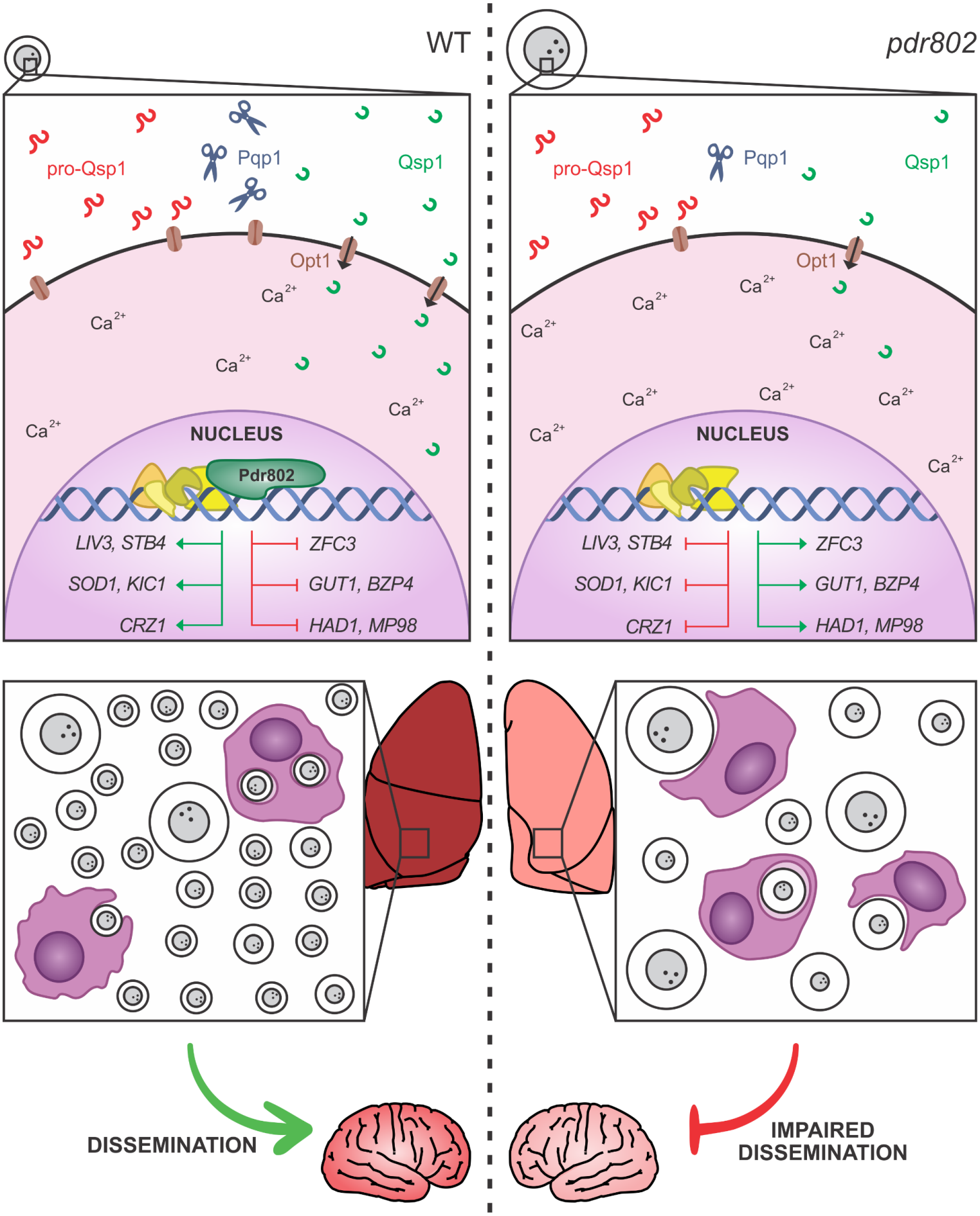
WT
pdr802
pro-Qsp1
Pqp1
Qsp1
Opt1
Ca2+
NUCLEUS
Pdr802
LIV3, STB4
SOD1, KIC1
CRZ1
ZFC3
GUT1, BZP4
HAD1, MP98
DISSEMINATION
IMPAIRED DISSEMINATION